Adv Polym Sci (2008) 212: 227–272
DOI 10.1007/12_2008_149

Published online: 13 June 2008

Structure and Morphology of Polyfluorenes in Solutions and the Solid State

Matti Knaapila[1] (✉) · Michael J. Winokur[2] (✉)

[1]Department of Physics, Institute for Energy Technology, P.O. Box 40, 2027 Kjeller, Norway
matti.knaapila@ife.no

[2]Department of Physics, University of Wisconsin, 1150 University Avenue, Madison, WI 53706, USA
mwinokur@wisc.edu

Abstract This account provides a state of the art overview of polyfluorene structure and phase behaviour in solutions and the solid state. This review covers key aspects of the hierarchical intra- and intermolecular self-assembly starting at the molecular level and extentding up to larger length scale structures. This includes crystallization, alignment on surfaces and texture. Many Central ideas are highlighted via structural archetypes. Recent theoretical treatments for understanding these structural properties are discussed and the implications for opto-electronics and photophysics are described.

Keywords Conjugated polymers · Polyfluorenes · Self-organization · Structure · Supramolecules

Abbreviations

$C_{12}E_5$	Pentaethylene glycol monododecyl ether
CP	π-Conjugated polymer
DOS	Density of states
ED	Electron diffraction
F2/6	9,9-Bis(2-ethylhexyl)fluorene
F8	9,9-Dioctylfluorene
F8BT	Poly(9,9-dioctylfluorene-*co*-benzothiadiazole)
F8T2	Poly(9,9-dioctylfluorene-*co*-bithiophene)
F8Ox	Poly{2,7-(9,9-dioctylfluorene)-*co*-1,4-(2,5-bis-(methyl-4′-(6-(3-methyloxetan-3-yl)methoxy)hexyloxy)benzene)}
GIXRD	Grazing-incidence X-ray diffraction
Hex	Hexagonal
HMW	High molecular weight
IXS	Inelastic X-ray scattering
LC	Liquid crystal
LMW	Low molecular weight
MCH	Methylcyclohexane
MEH-PPV	Poly(2-methoxy-5-(2-ethylhexoxy)-1,4-phenylenevinylene)
Nem	Nematic
NEXAFS	Near edge X-ray absorption fine structure
NLO	Nonlinear optics
PANI	Polyaniline
PBS-PFP	Poly{1,4-phenylene-(9,9-bis(4-phenoxy-butylsulfonate))fluorene-2,7-diyl}
PF	Polyfluorene
PF6	Poly(9,9-dihexylfluorene)
PF7	Poly(9,9-diheptylfluorene)
PF8 or PFO	Poly(9,9-dioctylfluorene)
PF9	Poly(9,9-dinonylfluorene)
PF10	Poly(9,9-didecylfluorene)
PF12	Poly(9,9-didodecylfluorene)
PF2/6	Poly(9,9-bis(2-ethylhexyl)-fluorene-2,7-diyl)
PFB	Poly(9,9-dioctylfluorene-*co*-bis-*N*,*N*′-(4-butylphenyl)-bis-*N*,*N*′-phenyl-1,4-phenylenediamine)
PDMOF	Poly{2,7-(9,9-bis((*S*)-3,7-dimethyloctyl))fluorene}
PMMA	Polymethylmethacrylate
PPP	Poly(*p*-phenylene)
PT	Polythiophene
PTFE	Polytetrafluoroethylene
SAED	Selected area electron diffraction
SANS	Small-angle neutron scattering
SAXS	Small-angle X-ray scattering
ssDNA	Single stranded DNA
SNOM	Scanning near-field optical microscope
TFB	Poly(9,9-dioctylfluorene-*co*-*N*-(4-butylphenyl)diphenylamine)
TFT	Tetrahydrofuran
XRD	X-ray diffraction

1 Introduction

In recent years conducting (or conjugated) polymers have become a key building block in the development of device technologies such as flat displays used in mobile phones and televisions. These materials are finding applications in areas as diverse as artificial muscles, electronic noses, plastic solar cells, corrosion inhibition, biosensors, electronic textiles, and nerve cell communications. This rapid evolution is based on the widespread advancements in (1) chemical synthesis of new materials, (2) new optoelectronics applications and (3) novel processing (e.g. ink jet printing). Consequently, the main streams of CP research comprise of synthetic chemistry as well as photo and device physics. However, the complex structures formed by these polymers are not thoroughly understood but this ordering underlies virtually all of the centrally important optical and electrical properties. Whether for enhancing a fundamental understanding of the optoelectronic properties, guiding the development of new device applications or providing new insight into the molecular design of new materials, it is critical to better understand their structural aspects and key structure–property relationships [1–3].

Apart from the emerging applications, the self-assembly of CPs is itself a fascinating subject. From the electronic perspective, these CPs represent a low-dimensional solid with strong covalent bonds along the molecular backbone and much weaker interchain interactions in orthogonal directions. The transport is therefore highly anisotropic and involves self-localized electronic excitations (e.g., solitons, polarons). Alternatively, from the structural perspective, the CPs are soft matter and belong to the class hairy-rod materials with a rigid backbone and flexible side chains [4]. Without the addition of functionalizing side chains the range of potential applications is limited. Linear, unsubstituted CPs (e.g., polyacetylene) exhibit very small increases in conformational entropy on dissolution or melting as well as a strong aggregation tendency. Consequently most of these materials are infusible and insoluble in common solvents. Functionalization via a side chain addition to the backbone forcibly dissolves the polar main chain in the surrounding matrix of a bound solvent and thus effects an attractive interaction between polymer and solvent. This leads to melting point depression and solution processability. In this context, the structural behavior of conjugated hairy-rods is understood in terms of self-organizing block copolymers [5] with rigid backbone and flexible side chains representing distinct blocks and forming microphase-separated domains. From another perspective these hairy-rods can be viewed in terms of thermotropic liquid crystals [6], and this liquid crystallinity stems from the highly anisotropic shape of the molecule.

There is an amazingly rich variety of CPs dependent on the choice of backbone and side chains and the nature of these two constituents has a major

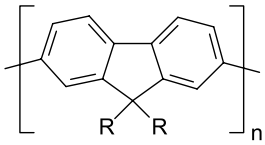

Fig. 1 Chemical structure of PF

influence on the phase behavior and resulting electronic and optical properties. Among the many reported CPs the PF family (Fig. 1) represents a central class of materials [7–10]. This emphasis stems from a combination of desirable qualities including facile synthesis, good environmental stability, excellent processing characteristics and efficient blue emission bands. There have been widespread efforts towards understanding, controlling and manipulating structures of PFs in both bulk and at surfaces. Not surprisingly, these advances have been exploited in a broad array of new polymeric technologies (for these optoelectronic aspects, the reader is referred to other reviews in this volume). These concerted efforts span multiple fields and those focusing on the structure attributes are widely distributed. No broad review of PF structure, assessing both the sold-state and solution, currently exists.

This review article focuses on the many levels of structural hierarchy ranging from the specifics of single PF molecules to those of aggregates in crystallites. The length scales span from Angstroms to tens of nanometers and beyond. The outline of the current review is as follows. First, we introduce the key structural attributes within single PF molecules. Next, we discuss the individual molecules and their aggregates in solution. Then we consider solid state and distinguish intra- and intermolecular structures including the higher levels of structural order in bulk, aligned fibers and aligned thin films. We also deal with similarities and differences between oligomers and polymers. Finally, we summarize and speculate on future studies. Overall this work spans the many landmark contributions in this quest to better understand PF structure.

2
Single Molecules

One of the guiding principles underlying much of the physics in conventional polymers is that many macroscopic macromolecular properties, not least the structure formation, can be satisfactorily understood even when the details of single molecules are ignored [11]. As is discussed later in this review, this idea still remains relevant for the intermolecular self-organization of hairy-rod PFs and for their macroscopic alignment. However, much of the behavior seen in PFs (and virtually all other electronic polymers as well) is an excep-

tion to this simplification because all optical and transport phenomena derive from the quantum mechanical properties of the base fluorene monomer and the near-neighbor coupling both along a single chain (i.e., intramolecular) and between chains (i.e., intermolecular).

While both intramolecular and intermolecule properties have relevance, it is often difficult to measure each independently. Two important settings that allow for direct observation of the single chain attributes are when isolated single polymers are dispersed on surfaces [12] or after dissolution of separated, uncorrelated chains in dilute solution. This latter topic is discussed in detail in the next section. The heterogeneous nature of the single chain structure in tandem with an overt sensitivity to the surrounding environment can, at times, make these very challenging systems to study. We expect that, with the advent of X-ray free electron lasers, direct structure studies of single molecules will become possible and this will resolve many key questions that still remain.

Single molecule spectroscopy of polyfluorenes [12] is discussed elsewhere in this volume and therefore we will limit our discussion of this matter. Many articles adopt the view that structure phase behavior and spectroscopic features can be strongly correlated. Clearly if a polymer chain is highly disordered one would expect there to be rather poorer transport properties and rather broad absorption and emission signatures. Parallels can be made to conventional diblock polymers in which highly ordered structures appear at relative large length scales but they still can be amorphous at nanometer distances. On the other hand in highly ordered materials the optoelectronic properties should be reflecting this fact [13, 14]. However, most conjugated polymers, PFs included, are intermediate between these two extremes and so the actual molecular level relationships are often subtle [15].

This subtlety is immediately apparent in direct comparisons of the chemically similar PF derivatives PF2/6 and PF8. PF2/6 (vide infra) is mesomorphic but the overall changes in the observed optical spectroscopy are quite modest. PF8 is also polymorphic but, in this case, there are very striking changes in the optical absorption and emission bands. Some of these may be associated with the formation of semi-crystalline phases and others not.

For both PF2/6 and PF8 the aforementioned main chain characteristics are essentially identical and so any pronounced differences are likely to originate in secondary structural characteristics of the functionalizing side chains. PF8 studies by Bradley and coworkers [16] first identified the unusual spectroscopic emission band now conventionally referred to as the "β phase". The hallmark signature of this peculiar chain structure is a relatively sharp series of emission bands red shifted some 100 meV from those seen when the polymer is prepared in a glassy state. π-Conjugated polymers have strong electron–phonon coupling and so, in addition to the π–π^* emission, there is a manifold of vibronic overtones spaced approximately 180 meV apart and red-shifted from the dominant π–π^* emission band.

The full PL envelope may be modeled using the Franck–Condon expression,

$$\mathrm{PL}\left(\hbar\omega\right) \propto [n(\omega)\hbar\omega]^3 \sum_{n_1=0}^{\infty} \cdots \sum_{n_p=0}^{\infty} \prod_{k=1}^{p} (1+c) \times \left[\frac{e^{-S_k} S_k^{n_k}}{n_k!}\right] \Gamma\left\{\delta\left[\hbar\omega - \left(\hbar\omega_0 - \sum_{k=1}^{p} n_k \hbar\omega_k\right)\right]\right\}, \quad (1)$$

where $n(\omega)$ is the refractive index, $\hbar\omega_0$ the π–π^* transition energy, and $\hbar\omega_k$ vibrational mode energies for each mode k with $n_k = 0, 1, 2, \ldots$ overtones. S_k is the Huang–Rhys coefficient (i.e., reflecting the strength of the electron–phonon coupling) and Γ is the lineshape operator (this is a function of the density of states, temperature and oscillator strengths) [17]. A similar expression may be used for photoabsorption but here the effects of heterogeneous broadening are more pronounced.

Modeling of the alkyl side chains in the two respective cases gives distinctly different outcomes (Fig. 2). On average the PF8 main chain adopts a more planar conformation and, additionally, one can differentiate three distinct families (denoted as C_α, C_β, and C_γ) of conformation isomers [17, 18] and correlate them with the variations in the observed PL spectra. In this

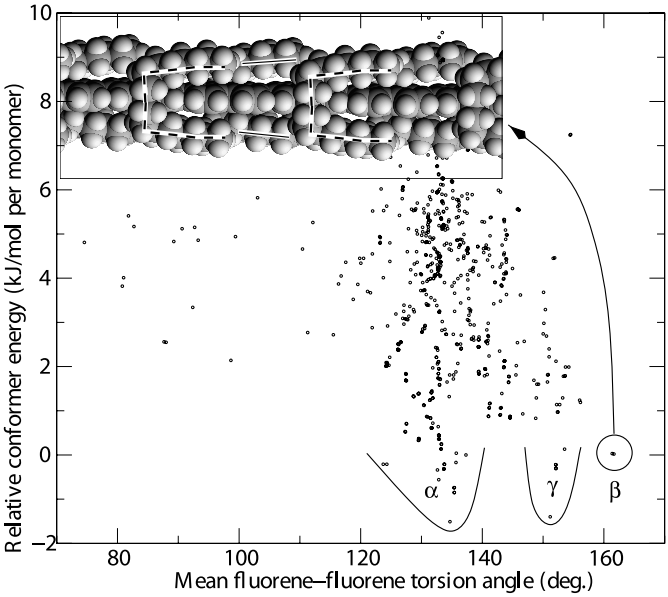

Fig. 2 Low-energy PF8 conformations (referenced to the C_β isomer). Each symbol corresponds to a single, unique tested conformation. C_α, C_β, and C_γ correspond to the conformer families. The *inset* shows the model of the C_β isomer highlighting side chains. Reprinted with permission from [17]. © (2005) by the American Physical Society

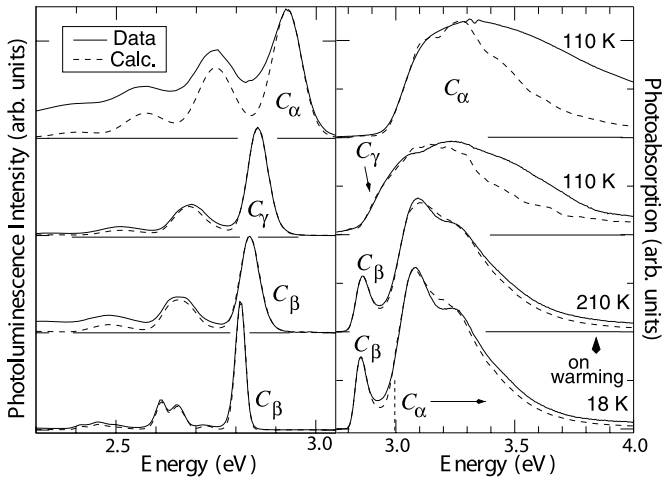

Fig. 3 Examples of PF8 PA and PL spectra from the three conformational isomer families in combination with calculated PL fits to the data using Eq. 1. Reprinted with permission from [17]. © (2005) by the American Physical Society

picture each family corresponds to a different ensemble average fluorene–fluorene torsion angle. As illustrated in Fig. 3 this trifurcation into conformational isomer families fully reproduces the PL experimental data when Eq. 1 is integrated with a tight-binding Frenkel-type exciton model. Guha and coworkers [19, 20] have shown that the differences in the side chain conformations are present in Raman scattering data and correlate well with ab initio quantum chemical calculations. From the perspective of single molecule spectroscopy each polymer chain is independently studied and its structure reflects one specific stochastic ensemble of main chain and side chain configurations in a self-consistent correspondence to the conformational energy surface topology.

3
Solutions

3.1
Structural Order of Polyfluorenes in Solution

PF solution studies are interesting for two chief reasons. First, PFs can be easily processed from solution and any structures adopted in solution will impact those that evolve in the subsequent processing. As might be expected, the solvent plays a major role in establishing the large length-scale morphology of solvent-processed PF thin films [21]. Second, the composition may

be continuously varied from isolated single molecules, in the dilute case, all the way to macrophase-separated domains and this provides a broad platform for pursuing studies of the fundamental physics.

Deciphering the main structural aspects of PF solutions is viewed as important but, so far, the published literature remains relatively sparse. Examples include PF8 [22], PF2/6 [23–25], F2/6 oligomers [26], and poly(9,9-dialkylfluorene-*co*-fluorenone) copolymers [27] in toluene as well as PDMOF in tetrahydrofuran [28].

The solution behavior of PFs may be subdivided in terms of three phenomenological variables—the nature of the solvent, the fraction of polymer, and the nature of the side chain. An additional parameter which becomes dominant in oligomers is the length of the molecule [26]. Once again PF8 can be highlighted as a prime example of a rich and variegated material. Its chain morphology has been detailed in different organic solvents such as chloroform, toluene, TFT and cyclohexane [29] and this work documents the striking structural diversity arising from the quality of the solvent, the first parameter in our discussion. For example, PF8 forms sheet-like particles in 1% (~ 10 mg/mL) solution in the poor solvent MCH but exhibits an isotropic phase of rod-like polymers at otherwise identical conditions in the better solvent, toluene [25, 30]. In addition, if the second parameter, the polymer fraction is increased from 1% to 3–7% (w/v) in toluene, individual PF8 molecules aggregate and form a large network-like structure [31]. A similar phenomenology is observed for F2/6 oligomers which adopt a rigid rod conformation in dilute toluene solution [26]. However, at concentrations in excess of 30 wt. %, a second dynamic process in the isotropic scattering function relates to clusters of rather spherical overall shape [26]. The effect of side chain length, the third variable, has been also studied for PFs in MCH at concentrations 1–5% (w/v) [32]. It has been found that the aggregation tendency of PFs decreases with increasing side chain length so that at room temperature PF10 with ten side chain beads adopts an isotropic phase. The limit of aggregation can be, once again, controlled by solvent quality. For example, the aggregation is prominent only for PF6 with six side chain beads if a better solvent, such as toluene is utilized [33].

Binary PF mixtures manifest several levels of structural hierarchy. The torsion angle between the monomer units represents the first level of this hierarchy. Wu et al. [28] studied PDMOF in THF and found a structure wherein each monomer unit adopted, at random, four rotational states. These were right- and left-handed torsional rotations of approximately 35 and 144° (consistent with either a 5/1 or 5/2 helices) and modest bond angle fluctuating (c.f., Fig. 4). At much larger distances, Rahman et al. [31] identified, in PF8, extended domain networks. The average distance between these aggregate domains is of the order of 60 nm (c.f., Fig. 5).

When mixed with MCH, PFs functionalized with linear *n*-alkyl side chains establish even greater levels of hierarchy. At room temperature, PF6, PF7, PF8,

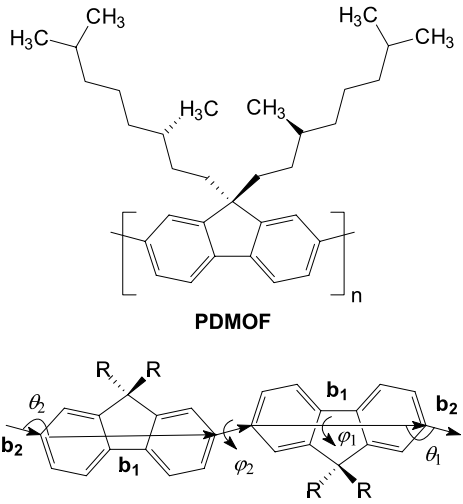

Fig. 4 Chemical structure of PDMOF and geometry of a polyfluorene derivative chain. Reprinted with permission from [28]. © (2004) by the American Chemical Society

Fig. 5 Schematic representation of the aggregate domains (*shaded area*) tying the PF8 chains to form a cluster. The overlap of the unassociated chains in the cluster as well as in the bulk of the semi-dilute solution generates a dynamic network with the characteristic mesh size of ξ_d. Reprinted with permission from [31]. © (2007) by the American Chemical Society

and PF9 form large (> 10 nm) sheet-like assemblies (thickness of 1–3 nm) which represent solution structure. Interestingly, the larger length scale structures of these sheets display a distinctive odd–even dependence on the side chain length—the PF6 and PF8 sheets are broader and thinner, whereas PF7 and PF9 sheets are thicker with a putative double layer structure. PF10 does not follow this sequence. Only a very small fraction of the polymer

assembles into a sheet-like structure and the rest remains dissolved at the molecular level (Fig. 6). Apart from PF10 these PF/MCH mixtures contain, at a shorter length scale, ordered "microcrystalline" structures having an internal period corresponding to the intermolecular periodicity of the solid state β phase of PF8. These domains may also act as nodes for establishing a network-like structure at large distances. The overall idea is illustrated in Fig. 7.

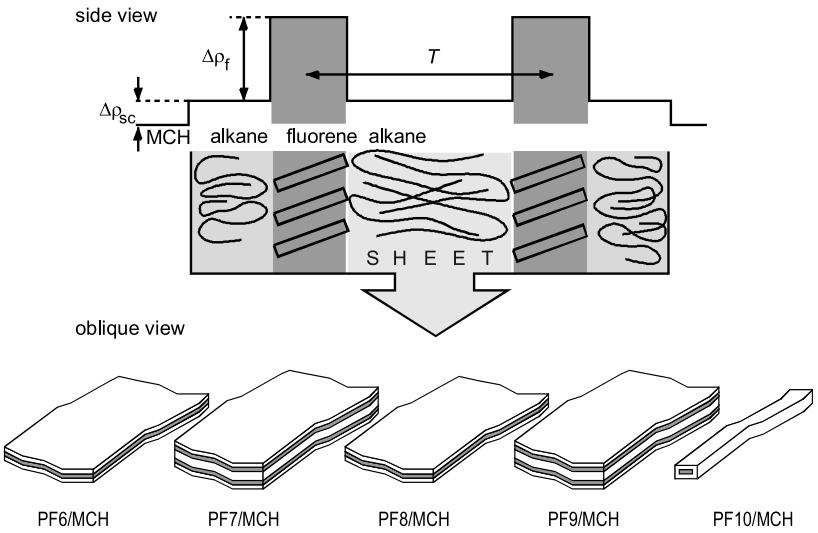

Fig. 6 Schematics of the proposed layer self-organization of PFs in MCH. Reprinted with permission from [32]. © (2007) by the American Chemical Society

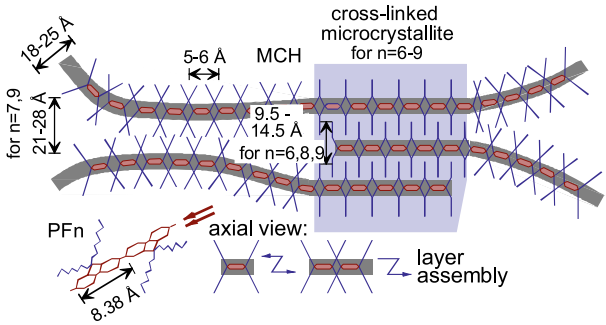

Fig. 7 Schematics of the possible structures of PFn with $n = 6.9$ in MCH. Loose lamellae correspond to those shown in Fig. 6. Reprinted with permission from [32]. © (2007) by the American Chemical Society

3.2 Water Solutions of Polyfluorenes

Water-soluble PFs are a new advance and these materials have opened the path for many new applications. These water-soluble CPs may be used with non-noxious, biocompatible solvents and have uses ranging from chemosensors [34] and biosensors [35] to inkjet processing [36]. Conferring water solubility to PFs is a challenging topic with few examples. One common strategy employed in order to achieve appreciable water solubility is the introduction of neutral or charged hydrophilic functionalities at the terminal position of the PF backbone. Development of this type of PFs has been pioneered by Bazan et al. [37–41] and they have used a number of different charged ammonium groups. This functionalization not only enhances solvent formation but also facilitates molecular recognition of biomolecules such as DNA and peptide nucleic acids. These PFs can be dissolved in high concentrations.

Wang et al. [42] have demonstrated that PFs with charged ammonium groups tethered at the end positions of the side chains, poly(9,9-bis{3′-((*N*,*N*-dimethyl)-*N*-ethylammonium}-propyl)-2,7-fluorene dibromide) are water soluble at concentrations as high as 100 mg/mL, cf., Fig. 8. Co-solvents such as methanol can be employed to ensure the uniformity of the solutions [43]. Another strategy for enhancing the solubility of PFs is to incorporate a surfactant layer separating the polymer from water

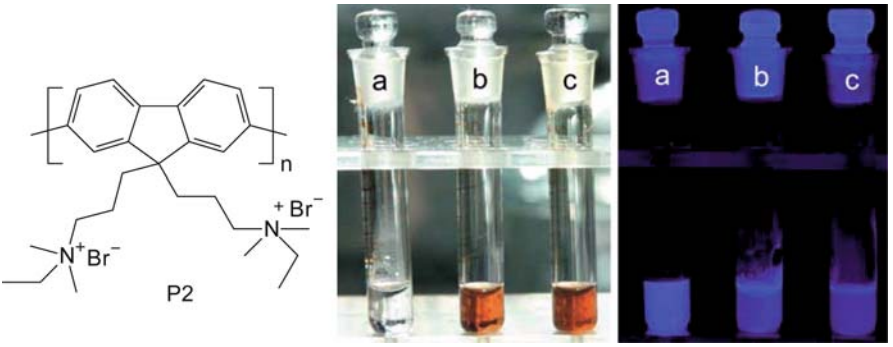

Fig. 8 *Left*: A chemical structure of poly(9,9-bis{3′-((*N*,*N*-dimethyl)-*N*-ethylammonium}-propyl)-2,7-fluorene dibromide) (P2). *Right*: A photograph of P2 with different concentrations in water (*left*). A photograph showing emission of light from P2 with different concentrations in water, the photograph was taken under irradiation with light at 365 nm (*right*). (a) Dilute solution (1×10^{-3} mg/mL), (b) 50 mg/mL, (c) 100 mg/mL. Reprinted with permission from [42]. © (2007) by Wiley-VCH Verlag GmbH & Co. KGaA

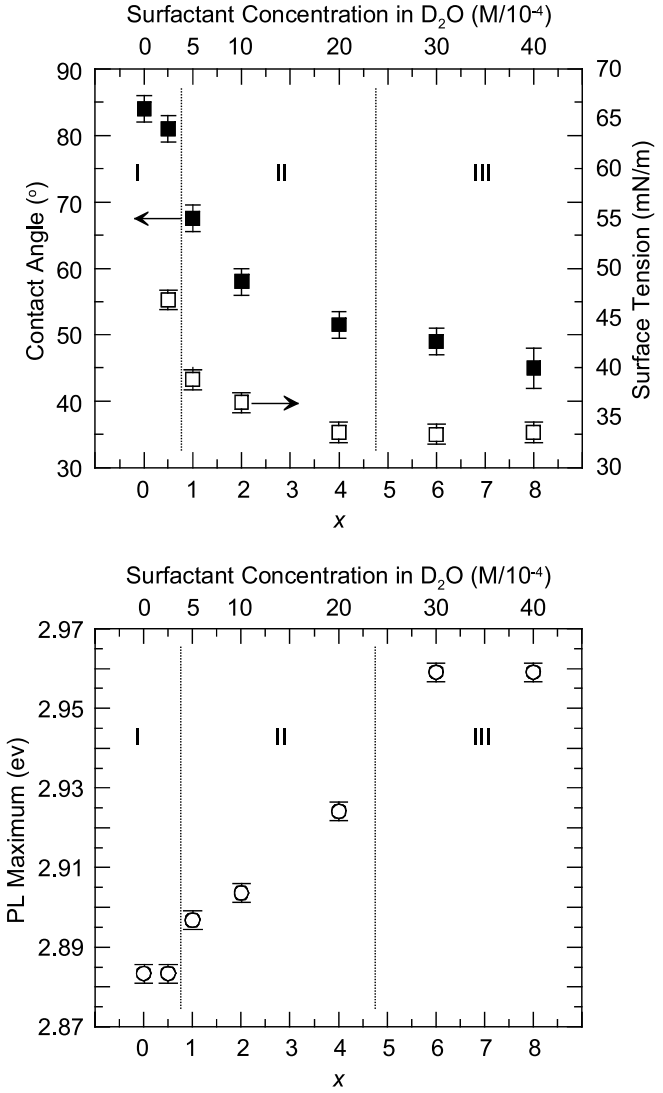

Fig. 9 *Top*: Contact angle (*solid squares*) and surface tension (*open squares*) of PBS-PFP in aqueous $C_{12}E_5$ as a function of molar ratio of surfactant over monomer unit *x*. The *dotted lines* distinguish tentative phase regimes I–III. $T = 20\,^{\circ}\mathrm{C}$. *Bottom*: Corresponding PL maxima. Monomer concentration was 5×10^{-4} M for all *x*. The *dotted lines* distinguish phase regimes I–III for which different solution structures are obtained. Reprinted with permission from [48]. © (2006) by the American Chemical Society

molecules [44]. The interaction between polymer and surfactant can arise from hydrophobic–hydrophilic effects [45], charge transfer [46], or molecular recognition [47].

Direct structural studies of these systems are scarce. In one example [48] PBS-PFP was studied in aqueous $C_{12}E_5$ as a function of molar ratio of surfactant to monomer unit, x, when the surfactant concentration was above the critical micelle concentration of aqueous $C_{12}E_5$ under conditions which corresponded to the isotropic liquid L_1 phase regime of the binary water–$C_{12}E_5$ system. Under these conditions, the following phase behavior is found by surface analyses (Fig. 9) and SANS (Fig. 10). The ternary solution is reported to be homogeneous when the polymer concentration is 5×10^{-4} M and the molar ratio of surfactant to monomer, x, is close to 1. This defines the first phase boundary. Elongated objects (of mean length ~ 90 nm) with near circular cross section (~ 3 nm) are observed for $1 < x < 2$. At sufficiently high surfactant concentrations, at $x = 4$, an interference maximum appears at $q \sim 0.015$ Å^{-1} in the SANS spectra and is indicative ordering by the micelles with a characteristic separation distance of 40 nm. This defines the second phase boundary. It is suggested that this ordering is due to electrostatic repulsion rather than steric hindrance.

Interesting analogies can be made with poly{9,9-bis(6-(*N*,*N*-trimethylammonium) hexyl)fluorene-*co*-1,4-phenylene} iodide mixed with aqueous $C_{12}E_5$ [49]. Al Attar and Monkman [50] probed the optical properties of this copolymer in the presence of ssDNA. In the system they found that poly-

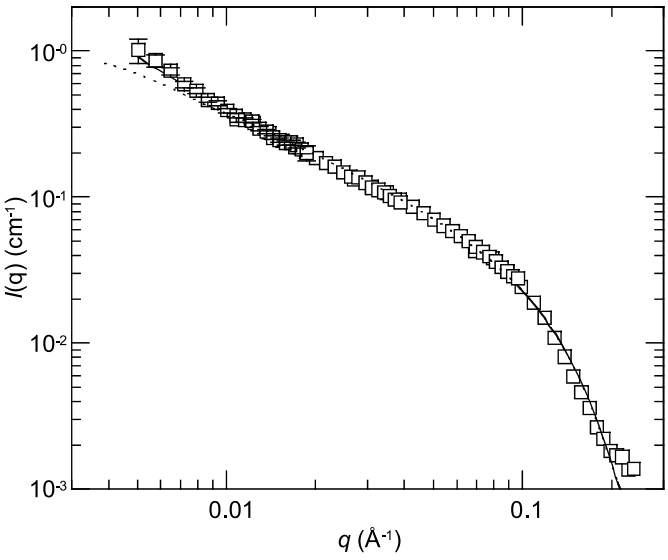

Fig. 10 SANS data of PBS-PFP copolymer with $C_{12}E_5$ surfactant in D2O. The monomer concentration was 5×10^{-4} M and the ratio of surfactant over monomer $x = 2.0$. Also shown are fits by flexible cylinder model (*solid line*) and stiff cylinder (*dashed line*). Reprinted with permission from [48]. © (2006) by the American Chemical Society

mer aggregation occurs only after the surfactant breaks down. They also observed that in solutions with low ssDNA concentrations the surfactant reduces quenching of the complex by preventing charge transfer processes. Charge transfer processes are sensitive to even small distance variations. They suggested that the reduced quenching stems from increasing the distance between the polymer and ssDNA by incorporation of polymer into aggregates. At high ssDNA concentrations the quenching actually *increased* sharply. This was attributed to the increase in the electrostatic force destroying the micelle's structure around the polymer.

4
Solid State

4.1
Intra- and Intermolecular Structures

4.1.1
Branched Side Chain PF2/6

Among the many PF derivatives that have been synthesized in recent years the branched 2-ethylhexyl functionalized polyfluorene, or PF2/6 [24, 51–56], clearly stands out as one of the two most heavily studied PF structural archetypes in both bulk and thin film form. The paper by Lieser et al. [51] is key and this work gives evidence for the formation of 5-fold helices through a combination of XRD, ED and molecular modeling. Additional support for this proposed main chain conformational motif is reported in follow up studies of PF2/6 [52, 53] and F2/6 [18, 57].

The modeling of [51] also emphasizes a very important PF *intra*molecular structural attribute; attention should be placed on the rotation between repeat units. In contrast to ladder-type PPPs [7] in which all phenylene rings are fused, PFs are representative of a "step-ladder" and this allows for a sterically hindered rotation between the repeat units. There is a well-defined competition between π-bonding, which lowers the total energy through planarization of the phenylene rings, and a steric repulsion of the α-hydrogens between adjacent monomers. Apart from a probable exception at very high pressures [58], PF2/6 usually adopts a stiff helical conformation of the main chain marked by a single ensemble average distribution of conformational isomers. Thermal cycling of PF2/6 leads to mesomorphic phase behavior with the presence of nematic, hexagonal and isotropic phases.

Modeling indicates the presence of multiple 2-ethylhexyl conformational isomers with nearly degenerate ground-state energies and a broad range of fluorene–fluorene torsion angles approximating the 144° angle necessary for

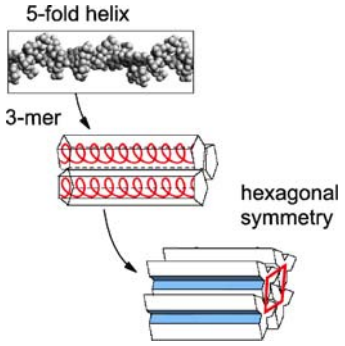

Fig. 11 Intra and intermolecular self-organization of PF2/6 polymer from 5-fold helices to a three chain ensemble and, finally, into an ordered hexagonal array. Adapted from [3]

a 5/2 helix (i.e., two full turns of the helix for every five monomers). Similar results are seen by Marcon et al. [18] in a molecular dynamics study. This heterogeneity leads to a PF material whose photoabsorption and photoluminescence of PF2/6 are, to first order, independent of the specific structural phase and subsequent processing.

In this picture the 5-fold helices constitute a base structure that self-organizes into triangular ensembles of three chains and these subsequently pack onto a hexagonal lattice at sufficiently high PF molecular weight and low enough temperature [24] (Fig. 11). This yield a semi-crystalline Hex phase with equatorial coherence lengths (i.e., the interchain packing) exceeding 20 nm.

An underlying issue with these helices is that the underlying 5-fold symmetry is incommensurate with the observed hexagonal unit cell and must introduce appreciable frustration. This latter effect will impact the crystalline perfection and any deviation from perfect periodicity introduces systematic effects in the Bragg scattering peak widths (and lineshape). Follow-up fiber XRD studies [24] identify a systematic trend in the observed scattering peak width consistent with the presence of paracrystallinity. Moreover, highly oriented PF2/6 fiber XRD data contains reflections which do not quite fit the nominal chain repeat specified by a 5-fold helix. Knaapila et al. [59] suggest that PF2/6 actually forms helices comprised of 21 monomers as opposed to the 5-fold helices, (i.e., in a 4×5 content) (Fig. 12). The 21-mer helical model would better accommodate the 3-fold rotational symmetry of the three chain unit cell and explain previously non-indexed reflections.

In regards to the *inter*molecular self-organization much can be learned from the physics of hairy-rod polymers [60] and PFs, especially PF2/6, are excellent model systems. As is the case in diblock polymers, a deceptively simple model parameterization of the key underlying interactions yields semi-quantitative predictions of the structural phase behavior. These model calculations can be directly compared to the experimental phenomena. The

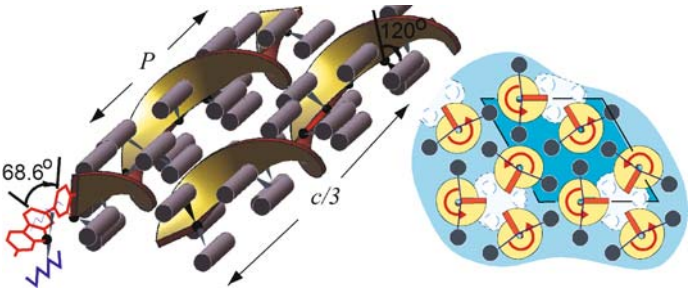

Fig. 12 Schematics of the helix form and side chain packing of PF2/6. In the proposed 21_4 helix the link atom is at the helical axis, around which the main chain and two side chains revolve quite like in a triple helix. The helical pitch P is defined by one complete turn of the backbone. The 21-helicity realizes 3-fold rotation symmetry. The *right* drawing shows possible arrangement of the side chains. The *dashed areas* correspond to sites unoccupied in this particular monomer layer. Reprinted with permission from [59]. © (2007) by the American Chemical Society

most extensive work describes the phase behavior of PF2/6 [24, 54, 55], as functions of both temperature and molecular weight, through a classic mean-field analysis of the free energies.

The main transition of interest in PF2/6 is a crossover from the Hex phase at high molecular weight to a Nem phase at low molecular weight, cf. Fig. 13.

In the mean-field analysis the free energy of the Nem phase is estimated as

$$F_{\mathrm{N}} \approx k_{\mathrm{B}} TVc \ln \frac{f}{\mathrm{e}} + k_{\mathrm{B}} TVc \ln \frac{4\pi}{\Omega_{\mathrm{N}}}\,, \tag{2}$$

where the first and second terms, respectively, correspond to the translational and orientational entropy. Here $k_{\mathrm{B}}T$ is the Boltzmann factor, V volume of the sample, c concentration of hairy-rod molecules, f the volume fraction of the backbone in the molecule, and e is the Euler number. The quantity Ω_{N} describes the degree of overall (uniaxial) alignment: The smaller Ω_{N} is, the more aligned the system.

In contrast, the Hex phase has negligible translational entropy and the interaction between ordered molecules due to the inhomogeneous distribution of side chain ends becomes dominant. The resulting free energy is

$$F_{\mathrm{H}} \approx k_{\mathrm{B}} TVc \ln \frac{4\pi}{\Omega_{\mathrm{H}}} - k_{\mathrm{B}} TV \frac{\nu}{\nu_0 l_{\mathrm{K}}^2 l_{\mathrm{u}}}\,, \tag{3}$$

where ν and l_{K} are, respectively, the volume and Kuhn length of a side chain, l_{u} is the distance between two consecutive grafting points (the length of the repeat unit), and ν_0 is the volume of one repeat unit of the hairy-rod.

The concentration c is directly related to M_n through $c = M_{\mathrm{u}}/\nu_0 M_n$ where M_{u} is the weight per repeat unit. For a given molecular weight and temperature, the phase with the lower free energy is more favorable. Thus, a threshold

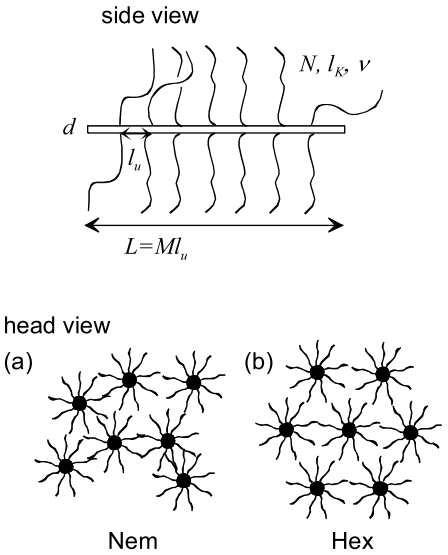

Fig. 13 *Above*: Schematics of a hairy-rod polymer consisting of a stiff backbone and flexible covalently connected side chains. N, l_{K}, and ν are the number of segments, the segment length (the Kuhn length), and the volume of the beds of the side chains, respectively; M, l_{u}, L, and d are the number of the repeat units, distance between grafting points (the unit length) and the length and diameter of the rod, respectively. *Below*: End-on schematics of (a) nematic (Nem) and (b) hexagonal (Hex) phase of hairy-rod molecules. Adapted from [24]

value, M_n^*, is obtained when the two free energies are equal

$$M_n^* \approx M_{\mathrm{u}} \frac{l_{\mathrm{K}}^2 l_{\mathrm{u}}}{\nu} \ln \frac{\mathrm{e}\Omega_{\mathrm{N}}}{f\Omega_{\mathrm{H}}} . \tag{4}$$

Equation 4 implies that for $M_n > M_n^*$, the Hex phase should be observed. Approximating $\Omega_{\mathrm{N}} \approx \Omega_{\mathrm{H}}$ which is justified near the glass transition temperature, the threshold molecular weight is given as

$$M_{n0}^* \approx M_{\mathrm{u}} \frac{l_{\mathrm{K}}^2 l_{\mathrm{u}}}{\nu} \ln \frac{\mathrm{e}}{f} . \tag{5}$$

The relation between molecular weight and degree of alignment can be estimated as follows [55]. PF2/6 is regarded as a hairy-rod molecule in which each chain consists of stiff segments of diameter d and length $l_{\mathrm{K}}^{\mathrm{HR}}$, where $l_{\mathrm{K}}^{\mathrm{HR}}$ is the Kuhn length of the rod (Fig. 14). The Kuhn segments are assumed to align independently, the total orientational configurational space for the

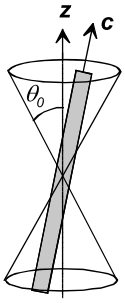

Fig. 14 The illustration of the alignment in 3D consideration. The vectors z and c represent the alignment direction and the backbone of a rigid molecule, respectively. Reprinted with permission from [55]. © (2005) by the American Chemical Society

chain being

$$\Omega_i(t) \approx \left(\frac{d}{l_{\mathrm{K}}^{\mathrm{HR}}} \left(1 + C_i t\right) \right)^{M_n l_{\mathrm{u}} / M_{\mathrm{u}} l_{\mathrm{K}}^{\mathrm{HR}}} , \tag{6}$$

where $t = T - T_{\mathrm{g}}$ is the temperature measured from the glass transition temperature T_{g} and C_i is a phenomenological coefficient which describes the change in the orientational freedom of a single segment with temperature. Subindices i = N, H refer to "Nem" or "Hex", respectively. When alignment between phases $\left(\Omega_i\right)$ is considered, the equation for the binodal T vs. M_n can be linearized to yield t as

$$t^* \approx A \left(1 - \frac{M_{n0}^*}{M_n^*} \right) , \tag{7}$$

where A incorporates all the phenomenological constants.

The implications of this theory are as follows: Eq. 4 yields a threshold weight separating a LMW, $M_n < M_n^*$, from HMW, $M_n > M_n^*$, regime. Equation 6 depicts the degree of alignment as a function of T and M_n. Equation 7 gives an approximate expression for the Hex–Nem coexistence line above T_{g}. When the experimental dimensions of the molecule are introduced into the theory, the Hex–Nem phase transition is predicted as a function of M_n. When $T^* \sim T_{\mathrm{g}}$, Eq. 5 predicts this transition at $M_{n0}^* \sim 10$ kg/mol for PF2/6 [24]. The limit in the case $M_n \gg M_n^*$ is obtained by the constant A extracted from experiment. Finally, the binodal, Eq. 7, is an interpolation between these limiting cases.

The phase diagram plotted in Fig. 15 compiles the theoretical result alongside experimental data for $T > T_{\mathrm{g}}$ [24]. For lower M_n only the Nem phase is possible above T_{g}. At lower T the Nem–Hex transition as a function of M_n is seen at M_n^* whereas the Hex–Nem transition as a function of temperature is observed for HMW materials. As seen in Fig. 15 the experimental data are in surprisingly good agreement with the theory although the theory only con-

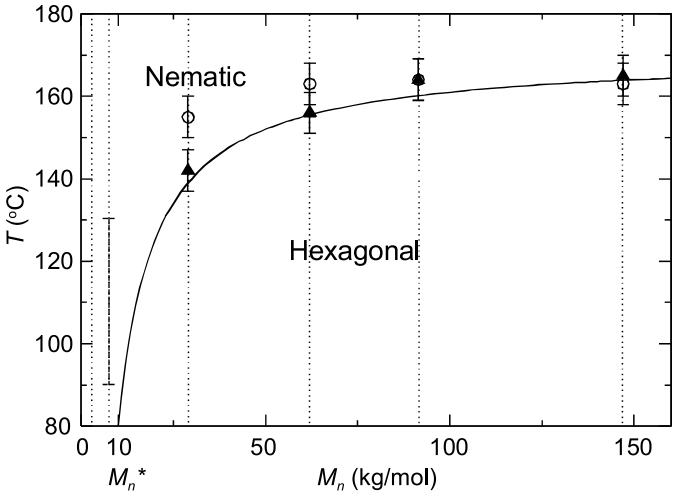

Fig. 15 Theoretical phase diagram of PF2/6 as a function of M_n for $T \geq T_g$ and the compilation of the corresponding experimental results. M_n^* defines low (LMW, $M_n < M_n^*$) and M_n high (HMW, $M_n > M_n^*$) regimes. The *solid line* shows the theoretical Nem–Hex phase transition. The Hex–Nem transitions based on DSC and XRD measurements are marked by *solid triangles* and *open circles*, respectively. The grid-lines correspond to the M_n of experimentally studied materials. The vertical bar at 90–130 °C for $M_n = 8$ kg/mol shows the position of occasionally seen Hex traces. Reprinted with permission from [24]. © (2005) by the American Physical Society

siders monodisperse chains whereas experiment contains polydisperse rods. What is not explicitly considered in this theory is the important fact that the hexagonal unit cell does not contain one but three polymer chains; a feature which stems from the 5-fold symmetry of the chain helical conformation. This suggests that the energy scale relating to the formation of three chains per unit cell is a comparatively small quantity. The mean-field approach itself is quite general and, with appropriate modifications, it is likely other CPs systems can be similarly understood.

Various PFs [61–63] and their pyrrole analogues [64] functionalized with chiral side chains exhibit NLO character and it is not clear how the chirality, helicity and NLO character are related. Because PF2/6 has become a model test system in the study of helical PFs, fully understanding its intramolecular structure can serve as a reference point for further comparisons. The molecular level heterogeneity intrinsic in the single chain structure of PF2/6 insures a high level of frustration and thus it represents a model polymer for paracrystals and paracrystallinity [24].

The near 5-fold helical symmetry of the main chains suggests a near pentagonal shape to the polymer chain and, with respect to interchain self-assembly of the Hex phase, the three-chain per unit cell is the basic packing motif for soft pentagons. This can be contrasted with the small two-fold reconstruction one

observes in packing of rigid pentagons (cf. [65]). Finally, we note that the above phase diagram holds only at ambient pressures and this is not the whole picture. Guha et al. [58, 66] have studied PF2/6 at high pressures by spectroscopic methods and found a phase transition involving a potential planarization of the chains at 20 kbar for the bulk and 35 kbar in thin film samples.

4.1.2 Linear Side Chain PF8

Linear side chain PF8 (or PFO) [17, 19, 20, 22, 67–76] represent another heavily investigated PF archetype and can be considered a counterpart to PF2/6. Apparent in all the reported findings to date is the conspicuous physical difference between these two materials despite their close chemical resemblance; they have a similar chemical stoichiometry and structure. The major distinguishing structural characteristics are the chain morphology and phase behavior. PF2/6, as already discussed, appears to be helical with nematic, hexagonal and isotropic phases. Single chain conformational studies indicate a broad distribution of conformational isomers whose inter fluorene–fluorene dihedral twist is approximately 45° [53]. Thus, photoabsorption and photoluminescence of PF2/6 are essentially phase independent. In contrast, as described in the single molecule section, PF8 is both more planar and more diverse, exhibiting upwards of three distinct conformational isomer families (denoted as C_α, C_β, C_γ) each with a different conjugation length and mean torsional angle between the monomers [17]. These intramolecular variations are paralleled by an increased level of interchain structures. PF8 is decidedly polymorphic with a crystalline α phase and meta stable crystalline α' phase, as well as amorphous, glassy, nematic and isotropic phases. Accordingly, the isomers and different "phases" of PF8 show significant photophysical differences despite their identical chemical make up.

In intermolecular (crystallographic) terms, the nematic and isotropic phase can occur at high temperatures (transitions at $\sim 160\,^{\circ}$C and $\sim 300\,^{\circ}$C, respectively) while it is generally accepted that at the room temperature the solid state is dominated by a stable crystalline α phase. This was first proposed to manifest a zigzag conformation with the fiber periodicity of 33.4 Å corresponding to four monomer units [67]. Later on, an orthorhombic lattice of eight chains with the space group $P2_12_12_1$ and lattice parameters $a = 25.6$ Å, $b = 23.4$ Å, and $c = 3.36$ Å (crystallographic **c** axis being along the polymer backbone) and theoretical density 1.041 g/cm^3 was proposed [73] (c.f., Fig. 16). This proposed picture was recently challenged by an alternative model based on a tetraradial construction of the side chains and a unit cell space group $Pnb2_1$ [76]. This model is illustrated in Fig. 17 and employs the following logic. At the onset PF8 was constrained to a planar zigzag conformation with, after accounting for the *n*-octyl sidechains, a four monomer periodicity along the **c** axis. In this model the planar backbone does not preclude the possibility of a left/right

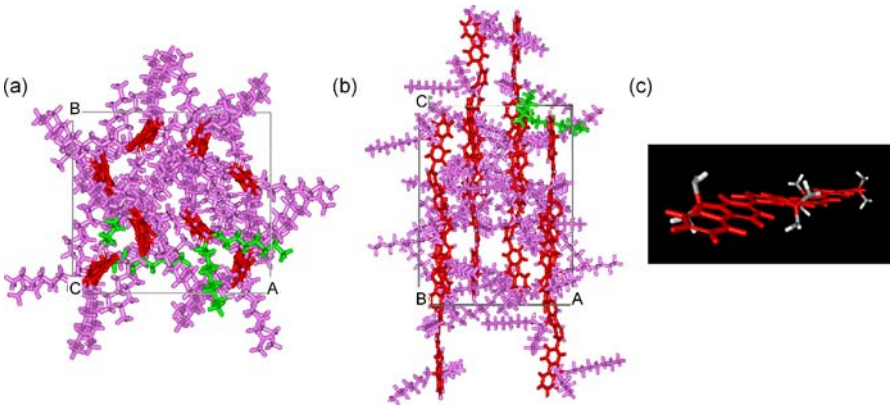

Fig. 16 Proposed model of molecular packing in the crystalline phase of PF8: energy-minimized structure (backbones in *red*) as viewed along **a** the **c** axis and **b** the **b** axis; **c** an expanded view with side chains hidden to demonstrate twisting of the backbone. A few selected pairs of *n*-octyl side chains are highlighted in *green* in (**a**) and (**b**) to allow for easier identification. Reprinted with permission from [73]. © (2004) by the American Chemical Society

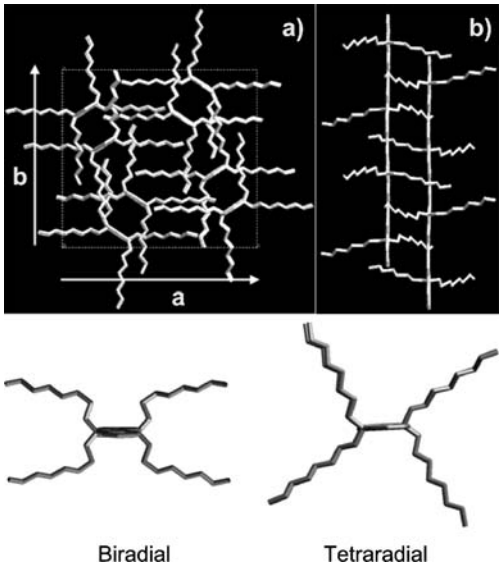

Fig. 17 *Above*: **a** **c** axis projection of the refined PF8 crystal structure. **b** Projection of the two-chain pattern along the 1–1–0 direction. *Below*: Projections of the PF8 chain conformation along the *c*-axis for the biradial and tetradial configuration of the *n*-octyl side chains. The hydrogen atoms are omitted for clarity. Reprinted with permission from [76]. © (2007) by the American Chemical Society

handedness for each PF8 chain and so, by invoking a systematic sequencing of either biradial and tetraradial side chain conformations [2], an efficient space filling packing of the *n*-octyl chains could be realized. Brinkmann [76] systematically examined a series of postulated packing schemes and found that the simulated SAED patterns compared most favorably with the tetraradial construction whose refined structure is shown in Fig. 17.

Another crystalline form, metastable α', is comprised of a slightly modified orthogonal lattice along the **b** axis ($b = 23.8$ Å) [75]. Non-crystalline room temperature phases include an (optically isotropic) amorphous phase and a metastable so-called β "bulk" phase (not to be equated with the C_β conformer and β-type optical emission). The overall phase behavior also includes a glassy g phase [12]. Even as complicated as this picture appears it still may be viewed as an oversimplification. A general depiction of the phase behavior is illustrated in Fig. 18.

Some special attention should be placed on the β (bulk) phase as well. Although this form is often reported as being non-crystalline, it gives rise to sharp Bragg reflections commensurate with lamellar order with a long period of 12.3 Å [74] and fiber periodicity of 16.6 Å (which corresponds to two monomer units) [67]. Thus, it differs from "real" crystals in the sense that it is mesomorphic. This phase also includes the presence of absorbed solvent and may be obtained by extended exposure to solvent vapor or solvent (cf., the solvent section). In particular, it has been found to appear as an intermediate step in the transformation from the solvent induced clathrate-like structure to the solvent-free well-ordered α phase [74]. The α and β (bulk) phases may coexist and are closed related to one another but are still structurally incompatible.

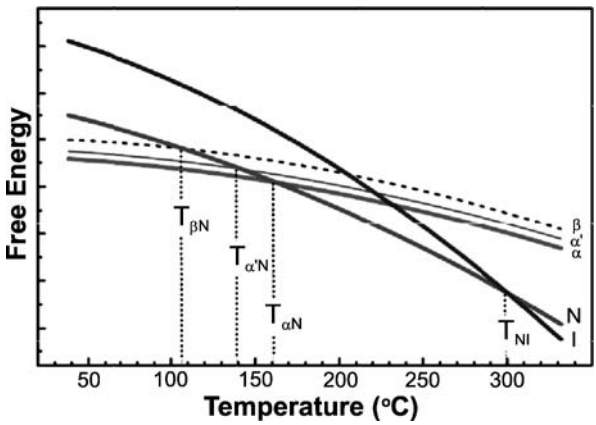

Fig. 18 Schematic free energy diagram, showing relative thermodynamic stabilities of various phases of solid state PF8. Reprinted with permission from [74]. © (2005) by the American Chemical Society

In regards to the intramolecular structure (as discussed in detail in the single molecule section) there may well be inhomogeneities in local structure arising from the side chain conformational isomerism (with either *anti* or *gauche* alkyl chain conformations). The three aforementioned conformational isomer families [17] reflect mean fluorene–fluorene torsion angles between adjacent fluorene monomers of approximately 135, 160, and 150° [17] (or 138, 165, and 155° [19]). Of these, it is the 150° (i.e., C_γ) conformer that is most likely to be incorporated into thermally annealed PF8 polymer samples (and thus be incorporated into the α crystal phase). Brinkmann's [76] planar model has many attractive structural qualities and the scattering data is noteworthy but this work includes no spectroscopic measurements and, without corroborating optical emission data, the backbone conformation in the PF8 crystal cannot be genuinely shown to be truly planar. It is also worth noting that the order–disorder transition observed at 80 °C (cf, Fig. 18) involves the loss of intra *and* interchain structural ordering [70].

4.1.3 Other Polyfluorenes

Apart from the above two examples, PF2/6 and PF8, the molecular structures and phase behavior of other PFs are known in far less detail. Two fluorene–thiophene copolymers, F8BT [77] and F8T2 [78], have been found to form lamellar semi-crystalline structures. An example of GIXRD data from a thin film F8BT sample is depicted in Fig. 19. Elsewhere the nature of the intra- and intermolecular interactions in F8BT have been studied by spectroscopic methods at elevated pressure [79]. As a general trend, by changing the side chain length, the interlayer spacing of a lamellar PF could be systematically changed [80].

Another interesting example is PF6 [81, 82]. Qualitatively PF6 exhibits many similarities to PF8 and the corresponding crystal phases are identified by Su et al. [81]. However, the structure is not identical and, while the α and α' phases of PF8 are both orthorhombic, the α and α' phases of PF6 are, respectively, monoclinic and triclinic. Interestingly, the analogous β "bulk" phase is characterized by a interlamellar periodicity of 14 Å and this is larger than that in PF8. The phase transition temperatures are also shifted and, while the nematic phase of PF8 appear at around 160 °C, the nematic phase of PF6 is not observed until at 250 °C [81].

4.1.4 PF Oligomers

Systematic structural studies of PF monomers and oligomers provide complementary structural information. Single crystal studies by Leclerc et al. [83] of 2,7-dibromo-9,9-dioctylfluorene-chloroform (or just the monomer it-

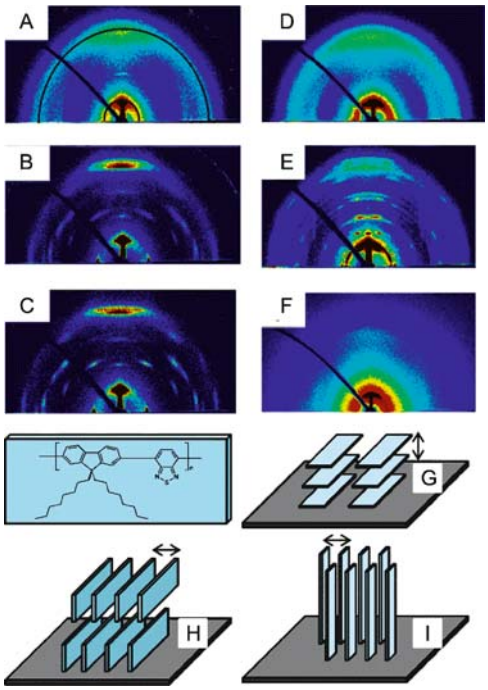

Fig. 19 GIXRD data for F8BT with molecular weight 255 kg/mol (**A**–**C**) and with molecular weight of 9 kg/mol (**D**–**F**). (**A** and **D**) Pristine, (**B** and **E**) annealed to T_g and slowly cooled, and (**C** and **F**) annealed to T_m and slowly cooled. The inner and outer rings in (**A**) correspond to the (001) and (004) reflections, respectively. The most likely orientations of the polymers with respect to the substrate is shown in (**G**), with the π-stacking direction indicated by *arrows*. Reprinted with permission from [77]. © (2005) by the American Chemical Society

self [84]), the base monomer of PF8, observe a planar fluorene core with the octyl side chains adopting an all *anti* conformation. A crystallographic study of the thiol-capped F6 monomer, 2,7-di(2-thienyl)-9,9-dihexylfluorene, by Destri et al. [85] yields similar results. This contrasts with the presence of *gauche* conformations in the PF polymers. With oligomers one can employ monodisperse samples and step-wise study the effect of increasing chain length of any number of properties.

Oligofluorenes studies have been performed by Wegner and coworkers [18, 57, 86, 87] and others [88, 89]. The packing frustration evident in the PF2/6 polymer is already present in the chains as short as a trimer [89]. Even at this short length thin films exhibit mesotropic-type phases [89] as opposed to the crystalline monomer samples.

A representative result is plotted in Fig. 20. While the intramolecular characteristics approximate those of high (molecular weight) PF2/6, the intermolecular assemblies of low molecular weight PF2/6 and F2/6 differ. As

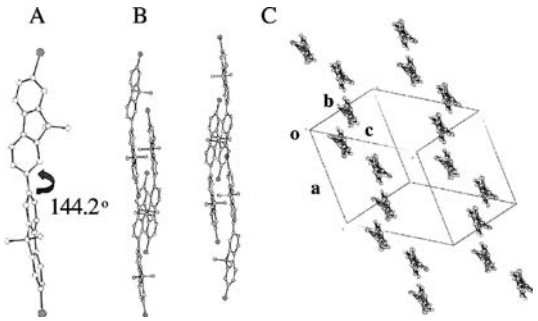

Fig. 20 The single crystal structure of (7,7′-dibromo-9,9,9′,9′-tetrakis(2-ethylhexyl)-2,2′-bifluorene) (or DBBF): **A** the aromatic framework shown without the aliphatic side-chains; **B** the chain packing showing the relation among the different molecules in the unit cell. **C** The 3D packing, projected along the molecular long axis. Note that the conformational angle between the two fluorene moieties in DBBF is 144.2°. Reprinted with permission from [57]. © (2005) by Wiley-VCH Verlag GmbH & Co. KGaA

discussed in the section above, LMW PF2/6 forms a nematic phase [24]. In contrast F2/6 oligomers develop a smectic B phase [57]. This difference arises from the fact that the PF2/6s are polydisperse whereas oligomers are monodisperse.

Another structural attribute that can be achieved in branched side chain PF oligomers are samples containing a single chiral enantiomer [88, 89]. These samples are intrinsically chiral and thus are optically active and can produce circularly polarized emission. Chiral functionalized PFs exhibit analogous properties [62, 63, 90].

Oligomers with *n*-alkyl functionalization have also received attention. A particularly intriguing question is in regards to the unusual β phase conformational isomer isolated PF8 and its presence in F8 oligomers. Tsoi et al. [91] confirm the presence of the β phase in very short oligomers but, by monitoring the emission energy as a function of chain length, estimate that its conjugation length actually extends up to 30 ± 12 monomers in longer oligomer samples. This observation of β-type emission in short oligomers reinforces the notion that the polymer crystal phases may not be directly correlated with the local conformational state of the polymer backbone.

4.2
Macroscopic Alignment of Polyfluorene Chains and Crystallites

4.2.1
Alignment

Achieving controlled macroscopic alignment of PF films is important for a wealth of reasons. Oriented samples exhibit anisotropic charge transport properties with enhanced mobilities and PF examples include F8BT [92],

PF8 [93], and F2/6 oligomers [94]. Major consequences also appear in the optical properties. In PFs the π–π^* transition dipole is arrayed nearly parallel to the chain axis and, in oriented samples, it is possible to achieve polarized EL or PL. This was demonstrated very early on in PF2/6 [95] and PF8 [96]. Here ellipsometry is an extremely useful analytical method and the optical constants of spin cast PF2/6 [97, 98] and F8BT [99] thin films have been widely measured. As-spun films exhibit strong optical anisotropy when probed with light having in-plane and out-of-plane polarization. S-Polarized light (i.e., in the plane of the films) undergoes a large absorption with a highly dispersive refractive index. Light polarized normal to the film surface experiences very low absorption and a weakly dispersive refractive index. These observations are consistent with a picture that within the as-cast films the polymer backbones are parallel to the surface but randomly oriented in this plane (i.e., a classic planar-type structure). Thermal annealing of PF films atop rubbed polyimide [97] lead to appreciable uniaxial alignment of the polymers parallel to the rubbing direction and this reorients the optic axis along the rubbing direction. This situation is also manifested in stretch-aligned PF fibers that have been prepared by mechanical drawing at temperatures above the glass transition temperature [24, 59, 67]. An interesting variation of this method employs mechanical stretching of a blend [100] (see the discussion of microfibers in the next section).

Advanced procedures to assess the extent of PF uniaxial alignment have been forwarded by Bradley et al. [101] but the nematic morphology intrinsic to PFs introduces significant secondary complications [102]. Although the majority of PF literature generally focuses on macroscopic alignment of the chain axes, it should be noted that large-scale structural anisotropy of CPs extends to directions [52, 103] orthogonal to the chain axis.

There are notable instances in which improvements in the structural characterization of aligned fibers has led to better understanding of the underlying optical properties. Galambosi et al. [104], for instance, were able to relate fiber XRD of PF2/6 to IXS and thereby present a unified theoretical and experimental treatment and the DOS arising from both the backbone and side chains. With aligned fibers they were able to identify directional components of IXS spectra and DOS.

Although uniaxial alignment within "bulk" fibers often provides a useful setting for more fundamental studies, a more technologically important format is that of a thin film. The presence of multiple interfaces and a large surface to volume ratio often introduces greater structural complexities and these derive from the surface interactions. In thin, uniaxially aligned PF films the stiff PF backbones collectively align locally into a domain and this ensemble, on average, lies in the plane of the film and the director points along a preferred in-plane axis. In the simplest case there is an oriented nematic phase. If, however, the PF chains also include long-range meridional and/or equatorial translational order, there can

be aligned smectic or crystalline phases. This leads to opportunities for a secondary alignment and is referred to as biaxiality. Biaxially aligned PFs manifest higher structural hierarchies in their textured crystallites (vide infra).

A common method for achieving uniaxial alignment of PF thin films is based on simply spin-casting of the CP onto a templating substrate (typically a rubbed polyimide layer). In regards to PFs, Miteva et al. [95, 105–109] performed much of the original work. Polyimide is electrically insulating and so if charge transport through the alignment layer is a necessity (i.e., in an LED device) the alignment layer can also be doped with an electroactive material [110]. The presence of a second component in the templating layer modifies the substrate/polymer interface and thus the nature of the unaxial alignment. The degree of chain alignment is a very strong function of system and process parameters. These include solvent [21] and polymer molecular weight [111].

Alternative methods, including friction transfer [71] and directional epitaxial crystallization [76], have also been used successfully in the alignment of PFs. In the friction transfer method one provides a crystalline templating substrate, (e.g., PTFE) and then applies a CP over layer. As in the case of a rubbed substrate, the CP does not significantly impact the orienting ability of the aligned substrate. This process is commonly referred to as graphoepitaxy.

Directional epitaxial crystallization requires a crystallizable solvent that is heated above its melting point and then exposed to a spatial thermal gradient that sequentially recrystallizes the solvent. As the temperature drops below the melting point the crystallizing solvent front conveniently functions as both a nucleating and orienting surface [76].

Anisotropic orientation of PFs may also have been achieved in LB films and by LB film transfer methods [112] but in this case uniaxial alignment has not as yet been achieved. Alignment can also be achieved using a top down approach rather than a bottom up strategy. Samuel and coworkers [113] used a rubbed polyimide surface coated with an intervening thermotropic liquid crystal layer to produce uniaxial orientation starting at the top surface of a PF2/6 LED device.

4.2.2 Aligned Films of PF2/6

PF2/6 films, depending on the explicit PF2/6 material and environmental conditions, can manifest uniaxial [54, 114] or biaxial alignment [52, 55, 115]. Figure 21 plots schematically an example of the uniaxial chain alignment (parallel to the substrate surface) and equatorial patterning (perpendicular to the surface) by LMW and HMW PF2/6 thin films atop templating rubbed polyimide substrates. In keeping with the terminology introduced above, the experimental observations are as follows.

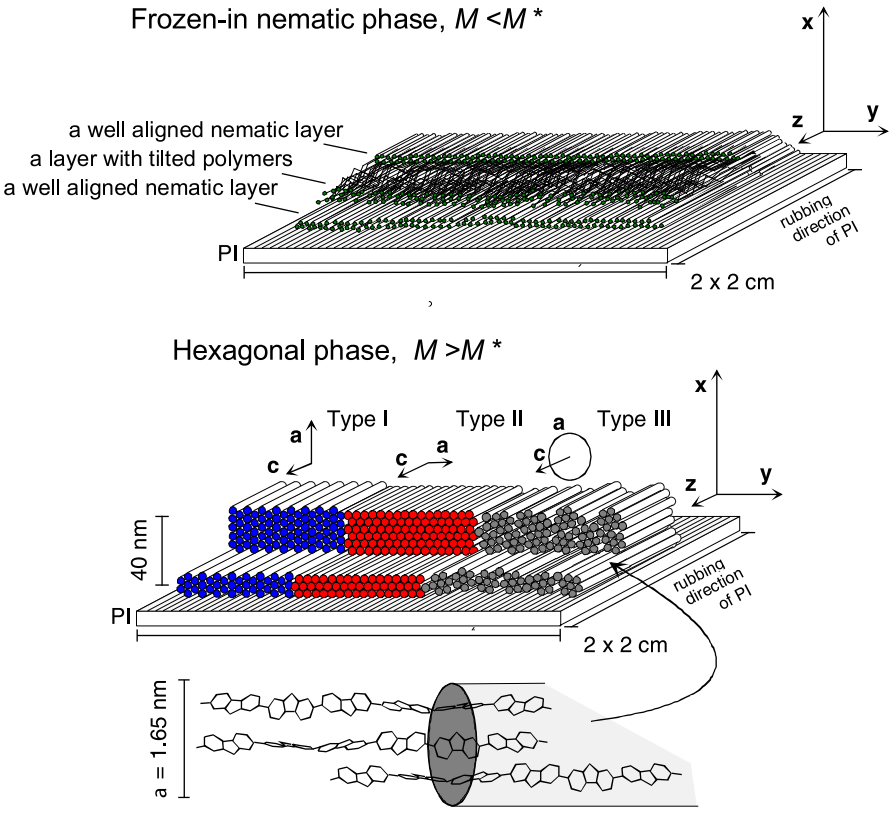

Fig. 21 Experimental geometry and schematics of the aligned PF2/6 films. *Above*: Uniaxially aligned frozen-in nematic PF2/6 microstructures. *Below*: Biaxially aligned hexagonal PF2/6 microstructures with crystallite types I–III. Assuming chain alignment (i.e., the c axis) along the rubbing direction, then the equatorial and meridional directions may be defined by the (*xy*0) plane and *z*-axis, respectively. See [114, 115] for details

Case 1: $M_n < M_n^*$. The structure of uniaxially aligned LMW PF2/6 has been recently studied by combination of optical spectroscopy, NEXAFS and GIXRD, Fig. 22 exhibits a representative NEXAFS data and the subsequent analysis. These data support a structural model in which there is a graded morphology such that the top and bottom surfaces exhibit extensive planar, uniaxial alignment while the film interior is less well oriented and includes both planar and tilted (i.e., non-planar) PF2/6 chains [114].

Case 2: $M_n > M_n^*$. Once the molecular weight exceeds a threshold value, M_n^* [24], PF2/6 forms hexagonal unit cells [51]. In this case the structure displays secondary effects due to the thin film geometry and the presence of interfacial forces. Here, there is a pronounced equatorial anisotropy with a measurable contraction of the lattice constants in the out-of-plane direction [52]. These surface interactions also give rise to a distinctive biaxial

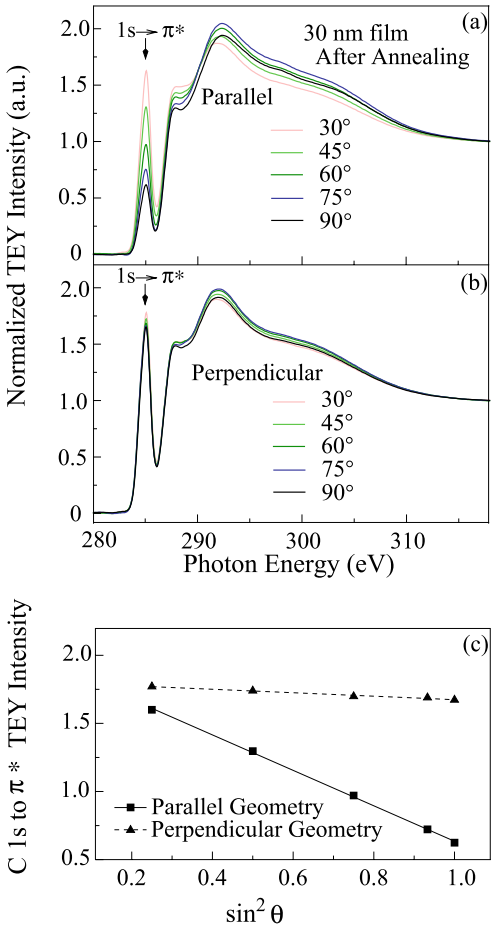

Fig. 22 Example NEXAFS data from an aligned PF2/6 film spin cast on rubbed PI. "Parallel Geometry" refers to *E*-field parallel to the rubbing direction. θ is the angle between surface normal and electric field vector of the incident light in conjunction with the rubbing direction of the polyimide substrate. See [114] for details

alignment marked by uniaxial (meridional) chain alignment and a multimodal equatorial anisotropy. In this situation the **c** axis is defined as the direction along the rod-like backbone (see GIXRD data in Fig. 23). The two dominant equatorial crystallite orientations, type I and II, have their respective **a** axes parallel and perpendicular to the surface normal [52]. These orientations form a mosaic texture and, in thin films, the crystallites extend through the entire thickness of the film [55]. These two equatorial orientations (i.e., type I and II crystallites) are also found to exhibit almost identical meridional orientation distributions [115] (Fig. 24). The equatorial ordering includes similar paracrystalline attributes in both the type I and II crystal-

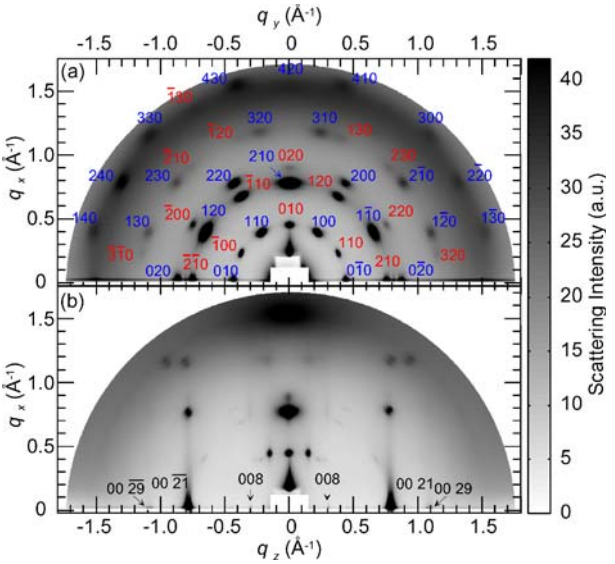

Fig. 23 GIXRD images from the PF2/6 film studied. **a** ($xy0$) plane, $\phi = 0°$ and **b** ($x0z$) plane, $\phi = 90°$. The GIXRD patterns were measured with the incident beam along the z- and y-axes, respectively. *Blue* and *red* indices show the primary reflections of the types I and II, respectively. Reprinted with permission from [115]. © (2007) by the American Chemical Society

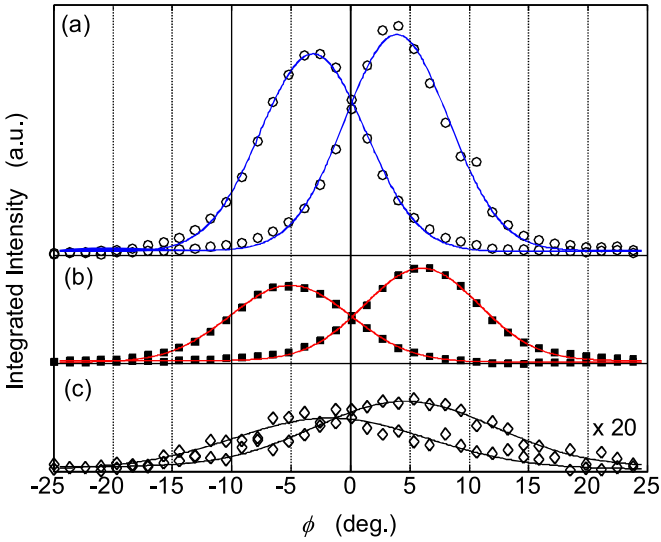

Fig. 24 Integrated intensities of the second hexagonal GIXRD reflections of aligned PF2/6 film corresponding to the sample of which the data is shown in Fig. 23. **a** Type I. **b** Type II. **c** Type III. *Solid lines* are corresponding Gaussian fits. Reprinted with permission from [115]. © (2007) by the American Chemical Society

lites. A small fraction of equatorial scattering is superimposed on a background of hexagonal phase polymer with a cylindrically isotropic orientation, denoted as type III [115]. This third type is most prominent in doped aligned films [116]. The overall model is thus summarized in Fig. 21.

The *uniaxial* PF2/6 alignment can be quantified in terms of the mean-field theory discussed previously. The degree of alignment in equilibrium (Ω) is a function of the number-averaged molecular weight (M_n) as described by Eq. 6. This prediction has been studied by photoabsorption in [55] and there it has been shown that the solid angle Ω is expressed in terms of the dichroic ratio in absorption (R) as

$$\frac{\Omega}{4\pi} \approx \frac{2}{R} + O\left(R^{-2}\right) , \tag{8}$$

where R is defined as

$$R = \left|\overline{E}_{\parallel}/\overline{E}_{\perp}\right| , \tag{9}$$

where $\overline{E}_{\parallel}$ and $\overline{E}_{\perp}$ are the maximum values of the absorbance for light polarized parallel and perpendicular to the **z** axis (cf., Figs 14 and 25). In a perfectly aligned sample the **z** axis is parallel to the molecular **c** axis.

Equations 6, 8, and 9 illustrate the relationship between phase behavior and Ω as a function of M_n. In particular, they imply that if Ω increases exponentially with M_n then, correspondingly, R decreases exponentially.

Figure 26 plots R from the PF2/6 films as a function of M_n when the uniaxial alignment has been allowed to reach saturation (at elevated temperature) in the Nem phase regime (cf., Fig. 15). The overall picture for the alignment under similar conditions is that the degree of alignment first increases (R linearly) and then drops (R exponentially) with M_{n}·. So LMW PF2/6 behaves quite differently than the HMW material, not only in terms of self-assembly but also in terms of the overall alignment.

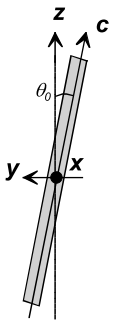

Fig. 25 The illustration of the alignment in a 2D consideration. The vectors z and c represent the alignment direction and the backbone of a rigid molecule, respectively. Reprinted with permission from [115]. © (2007) by the American Chemical Society

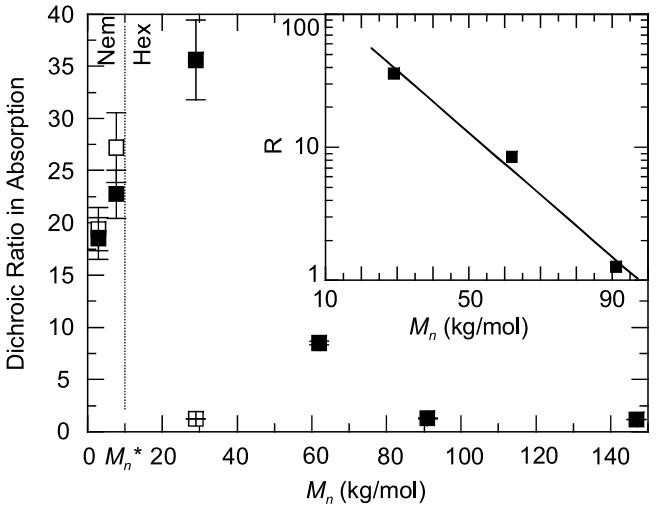

Fig. 26 Dichroic ratios in absorption (R) as a function of M_n as measured at 380 nm. The *open squares* correspond to the samples annealed at 80 °C for 10 minutes and the *solid squares* those at 180 °C for 18 h. A *dotted line* shows M_n^*, the Nem–Hex transition point of PF2/6. An *inset* shows the region of an exponential drop between $M_n = 10^4$–10^5 g/mol and a linear fit. Reprinted with permission from [55]. © (2005) by the American Chemical Society

The maximum degree of alignment as a function of M_n is achieved at the boundary of these regimes, at around $M_n^* \sim 10$ kg/mol. These regimes have been characterized as follows [55].

- $M_n < M_n^*$: The small LC regime, regime 1. Because the lengths of molecules in the regime 1 are approximately twice the persistence length [23], flexibility is not dominant and therefore the alignment increases with M_n [117].
- $M_n > M_n^*$: Chain flexibility now becomes important. If inflexible, the molecules in the melt would align perfectly apart from thermal fluctuations. As predicted by Eq. 6, the flexibility changes the Ω scaling as $\Omega \sim (\text{const.})^{M_n}$. An exponential increase in Ω implies an exponential decay in R. This is experimentally confirmed between 10–100 kg/mol in the inset of Fig. 26.
- $M_n \gg M_n^*$: R reaches its minimum (i.e., it cannot decrease further from unity).

Although the alignment is discussed under the assumption of a Nem phase, the same progression holds for the Hex phase with one exception. There is no regime 1 because the Hex phase does not exist when $M_n < M_n^*$.

These above concepts do not differentiate between which crystallite types actually exist in PF2/6 films (see Fig. 21). The connection between uniaxial

and biaxial orientation of crystallites has been described in [115]. In this example R is first related to the 2D orientational order parameter s with

$$s = \frac{R-1}{R+2} \,. \tag{10}$$

The order parameter s links R to the mosaic distribution of the azimuthal rotation angle about the surface normal (ϕ). The former is measured using optical absorption spectroscopy whereas the latter is measured separately for each crystallite types using GIXRD. In this task it has been assumed that the rod-like molecules are always parallel to the (0yz) plane (i.e., perfectly planar alignment) and a two-dimensional order parameter can be given as

$$s = \left\langle 2\cos^2\theta - 1 \right\rangle = \int f(\theta)\cos 2\theta \, \mathrm{d}\theta \,. \tag{11}$$

At a high degree of orientation, this may be simplified by $\cos\alpha \simeq 1 - \alpha^2/2$

$$s \simeq 1 - 2\theta_0^2 \,, \tag{12}$$

where $\theta_0 = \sqrt{\langle\theta^2\rangle}$ may be physically interpreted as the angle accessible for the rotational motion of a molecule (see Fig. 25).

In one experimental test case [115] R corresponded to measured values $\theta_0 = 11°–15°$. These numbers were then compared to those obtained by GIXRD. For the three crystallite types I–III respective values of $\theta_0^{\mathrm{I}} = 8.8 \pm 0.2°$, $\theta_0^{\mathrm{II}} = 9.9 \pm 0.2°$, and $\theta_0^{\mathrm{III}} = 15 \pm 1°$ were observed. The difference between the GIXRD and optical measurements stems from the fact that GIXRD is preferentially sensitive to crystalline material. To reconcile this difference it was necessary to include a non-crystalline volume fraction of $g_{\mathrm{nc}} \simeq 0.06…0.12$; a value which was comparable to the value estimated from diffuse scattering ($\sim 10\%$).

4.3 Surface Morphology

The surface and interfacial morphologies within CP films and their blends are clearly an extremely important aspect of many device applications in which charge generation and energy transfer are key (e.g., see [118–120]). The morphology of many PFs is well-known and PF8 surfaces, for example, often consist of nanometer-sized crystalline grains [73, 76]. Ample studies have shown that the surface quality of the PF films is a strong function of both the processing conditions and the explicit functionalization. The molecular level attributes already discussed, such as chain length, side chain branching, and molecular weight, are equally important in establishing the interfacial structure.

Teetsov and Vanden Bout [121–123] have used SNOM to study linear side chain PFs as a function of side chain length. These authors found polymer-

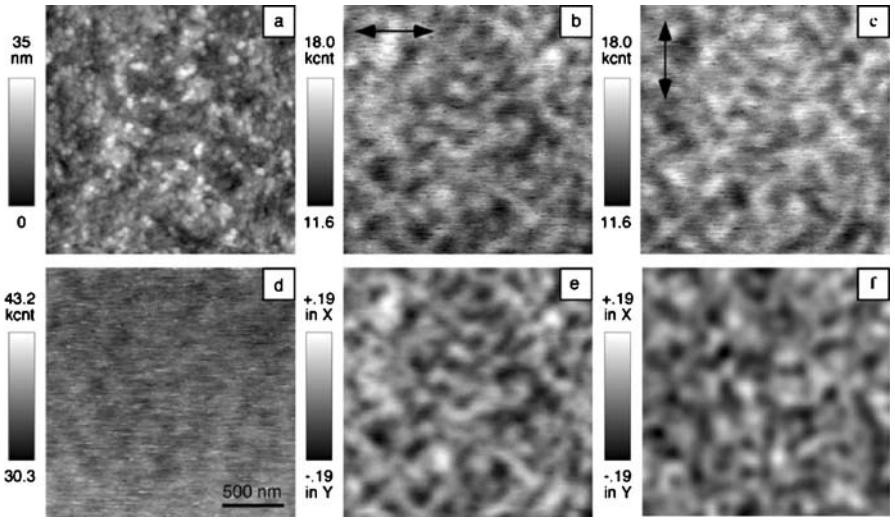

Fig. 27 $2 \times 2\,\mu$m SNOM images of annealed films of PF6 (**a** and **d**), PF8 (**b** and **e**), and PF12 (**c** and **f**): topography (**a**–**c**) and SNOM fluorescence anisotropy (**d**–**f**). Reprinted with permission from [122]. © (2002) by the American Chemical Society

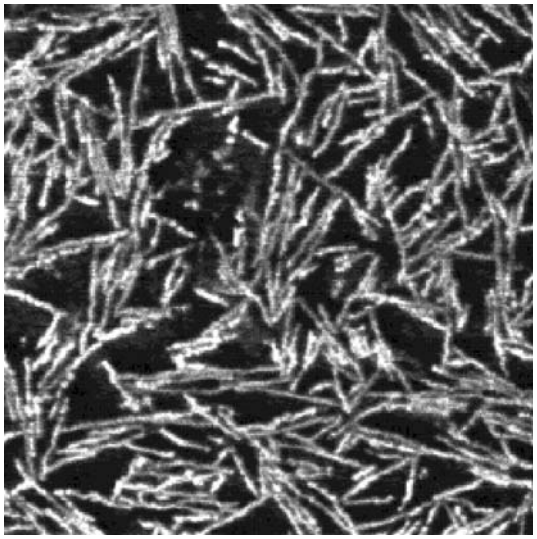

Fig. 28 Tapping mode AFM phase images of a thin PF8 deposit on mica. The area is $1.0 \times 1.0\,\mu$m. Reprinted with permission from [124]. © (2002) by the American Chemical Society

specific ribbon-like domains 15–30 nm in size. An example is shown in Fig. 27. As a result they concluded that it was the molecular scale interchain interactions that were ultimately responsible for these systematic variations in the morphology.

Surin et al. [124] studied several PF films on mica and reported that the microscopic morphology is also strongly correlated with the molecular architecture. PFs with branched side chains revealed a smooth featureless surface down to the nanometer scale whereas PFs, with linear side chains, formed networks of fibrillar structures in which the chains are closely packed. An example of PF8 fibrilles is shown in Fig. 28.

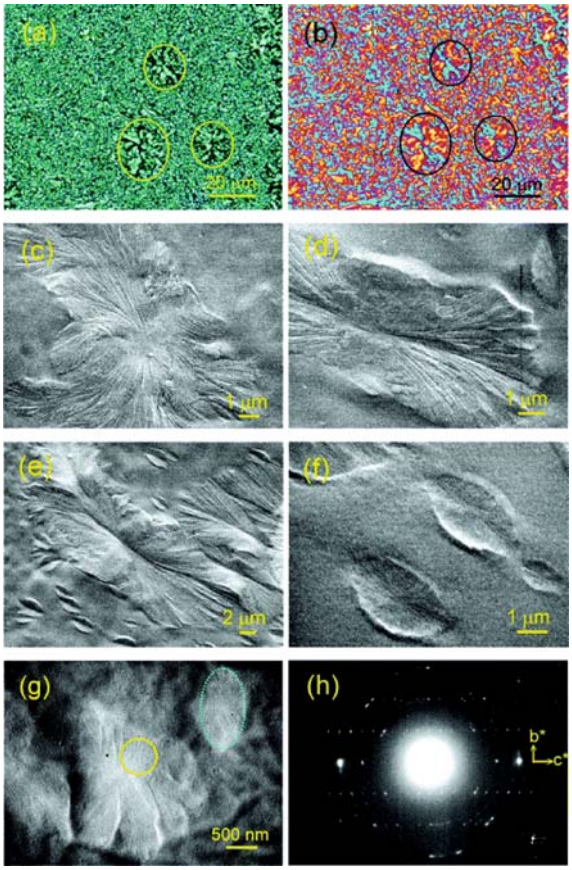

Fig. 29 Axialitic morphology of PF8 films melt-crystallized for 6 min at 145 °C , followed by a rapid cooling: **a**,**b** Polarized micrographs without or with gypsum plate inserted, **c**–**f** Secondary electron images at several locations under different magnifications, and **g** a representative BFI and **h** the corresponding SAED pattern. The axialites first appear as leaf-like entities (**f**), which grow and splay mainly in the axial direction (**d**) and become less anisotropic with transversely nucleated branches (**c**). A representative BFI image (**g**) and the corresponding SAED pattern (**h**, taken from the axialite at the central view, slightly rotated to align the b^*-axis with the meridian) indicate that molecular chains run transverse to the long axis of fibrillar features that correspond to slender edge-on crystalline lamellae. Note the presence of a junior-axialite in the *upper right* corner of (**g**). Reprinted with permission from [125]. © (2006) by the American Chemical Society

The surface morphology of aligned F8BT [111] and PF2/6 [56] films have been studied as a function of molecular weight. In the case of PF2/6 there is a crossover in the surface morphology between smooth (Nem phase with $M_n < M_n^*$) and rough (Hex phase, $M_n > M_n^*$) at the threshold molecular weight M_n^* [56]. The domains at the PF2/6 surface appear as aligned furrows and ridges with dimensions comparable to the crystallite size as obtained by XRD.

The examples reported in [56, 111] were of samples achieving a high level of uniaxial alignment. These films were annealed for several hours over which it was assumed that equilibrium had achieved. Far more variegated features are seen to develop during thermal annealing. Chen et al. [125] studied PF8 films from rapid quenching up to some minutes of thermal annealing. They identified a rich interplay of asymmetrically growing spherulites or axialites. These objects were composed of slender edge-on crystalline lamellas with the preference of growth in the axial direction (see the richly textured images in Fig. 29).

4.4 Higher Levels of Complexity—Nano and Microscale Assemblies

4.4.1 "Bottom-Up" Nanostructures

There is a wide range of so-called bottom-up methods for achieving complex structural hierarchies within polyfluorene nanostructures. Synthesis of block

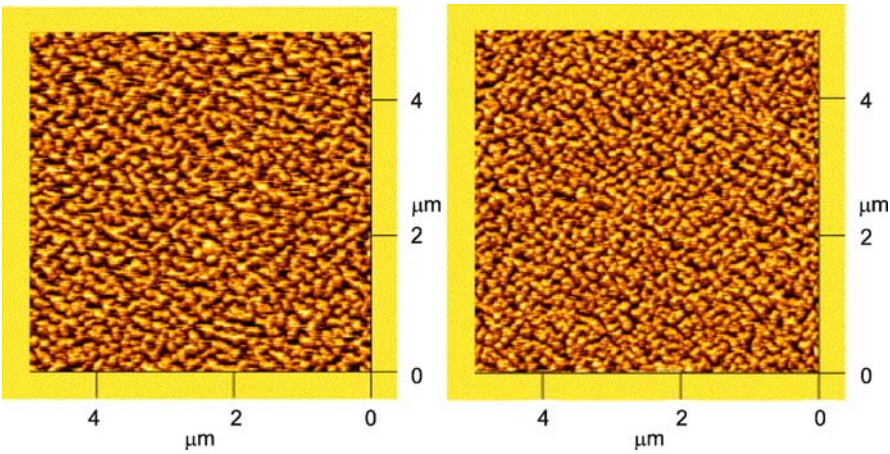

Fig. 30 AFM images (tapping mode) of thin films of the PF-*b*-PANI triblock copolymers. PF is equipped with 3,7,11-trimethyldodecyl and PANI with undecyl side groups, which have been spin-coated from two different solvents: (*left*) chloroform and (*right*) toluene. Reprinted with permission from [126]. © (2005) by Elsevier

copolymers represents one obvious approach for introducing additional competing interactions at the molecular level. Examples of microphase-separated structures of PANI/PF/PANI and PT/PF/PT triblock copolymers have been reported by Scherf and coworkers [126]. The polymers formed segregated domains of sizes ranging from 50 to 300 nm. One example is shown in Fig. 30. In these films the segregation can be controlled by the solvent. This allows selective tuning of the photoluminescence quenching [127]. Elsewhere, Jenekhe and coworkers [128] have combined PF2/6 with poly(γ-benzyl-L-glutamate). These three articles represent just a small slice of the types of materials that can be synthesized and self-assembled.

PF blends provide another clear route for controlling the nanoscale domain architecture. Unlike block copolymers, in which phase separation is constrained by chemical bonds, with blends one can adjust the conditions all the way from complete miscibility to macrophase separation. Examples of dir-

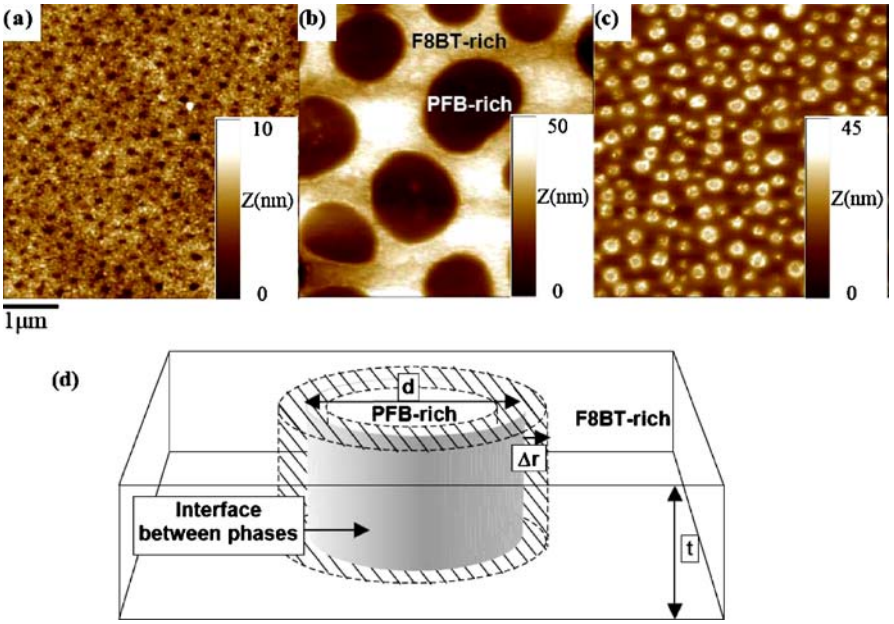

Fig. 31 AFM images for thin films of PFB/F8BT blends with ratios: **a** 1 : 5, **b** 1 : 1, and **c** 5 : 1. **d** 3D schematic representation of blended polymer film. The PFB-rich phase is represented by the volume within the *dark gray cylinder* and the F8BT rich phase is represented by the *hollow box* on the outside of the *dark gray cylinder*. Photogenerated charges within a thin cylindrical shell (*light gray region*) about the interface between the two mesoscale phases (*dark gray cylinder*), become collected charge at electrodes. t is the film thickness, d is the average diameter of the circular phase, and Δr is the distance over which charge can migrate, within the minor phase, to reach the interface. Reprinted with permission from [119]. © (2002) by the American Chemical Society

ect imaging of this segregation include a blend of PF8 and polystyrene [129], PF8 and PMMA [130], F8BT and PFB [131], F8BT, PFB, and TFB [132] or PF8 and F8BT [133–135]. A prominent example of the technological implications is shown in work by Friend et al. [119]. Here they analyzed the impact of varying composition and segregation in a PFB/F8BT blend in a series of photovoltaic devices. Examples of the observed morphological structures are shown in Fig. 31. The PFB and F8BT, respectively, function as hole- and electron-acceptors in the photovoltaic device and the quantum yield is strongly composition dependent. Moreover, Friend and coworkers showed that charge-transport was the main factor limiting the device performance and, additionally, demonstrated that this can be optimized by controlling the microphase separation.

There are examples demonstrating higher level structural order in PF networks through solution chemistry and gel formation (c.f., Fig. 5). In these cases the assemblies are based on cross-linked microcrystallites and physical bonding [31]. Covalently cross-linked PFs have also been introduced in the solid state [136–138]. Cross-linking, by means of photopolymerization of F3 or F7-containing LC oligomers, has been used to control charge carrier mobilities [137]. A cross-linkable F8Ox copolymer has been used in the fabrication of multilayer LEDs [136]. In this example the cross-linkable layer was utilized in multilayer fabrication to separate poly(3,4-ethylenedioxythiophene) and F8BT. Although extensive structural studies are not yet reported, we believe this is certainly another topic area in which in-depth structure studies would be beneficial.

4.4.2 "Top-Down" Nanostructures

Complementing the bottom-up methods which rely on competing molecular interactions are a number of "top-down" approaches for producing PF nanostructures. An intriguing microporous template-based method has been developed by Redmond and coworkers using either F8T2 [139] or PF8 [140–142] to prepare nanowires. In this method the bulk polymer, PF for example, is deposited onto the surface of a porous anodic alumina membrane having a typical pore size of a few hundred nanometers. Then the system is thermally annealed, often with applied pressure, to induce pore filling. Excess polymer is removed mechanically after it solidifies on cooling. Thereafter, the PF nanowires are released by soaking the template (typically in aqueous NaOH which etches away the template). Finally, the wire residue is washed with water and suspended in decane. Examples of these nanowires are shown in Fig. 32. Optical emission studies can identify polarized emission indicating that the PF chains tend to align parallel to the wire axis. This method can allow also for preparation of hollow PF nanotubes [142] (c.f., Fig. 33). These kinds of nanowires can be subsequently aligned on films. These authors have

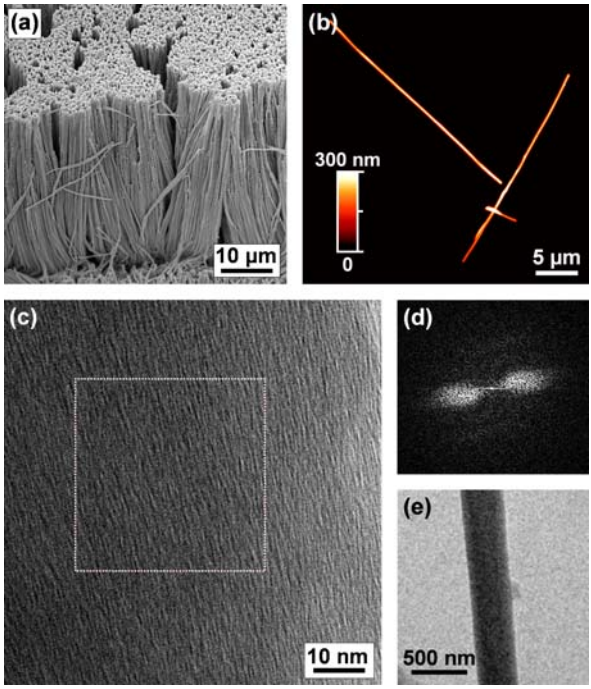

Fig. 32 **a** SEM image of a melt wetted PF8 nanowire array following template removal. **b** Tapping-mode AFM image of nanowires on a glass substrate. **c** High-resolution bright-field TEM image of a nanowire region. **d** 2D FFT of the region of the image indicated by the *white rectangle* in (**c**). **e** Lower magnification TEM image of the wire. Reprinted with permission from [140]. © (2007) by Elsevier

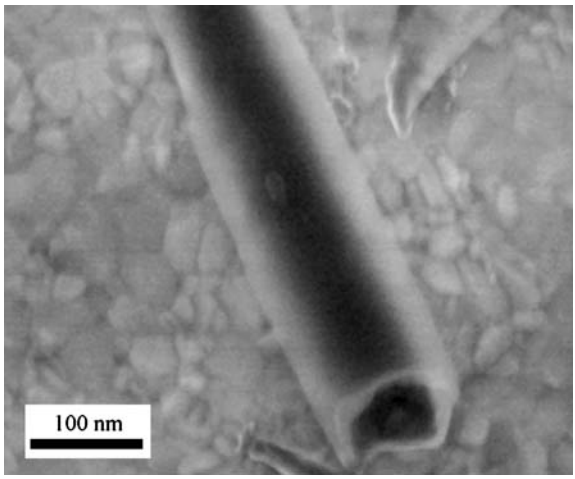

Fig. 33 SEM image of a PF8 nanotube. Reprinted with permission from [142]. © (2008) by the American Chemical Society

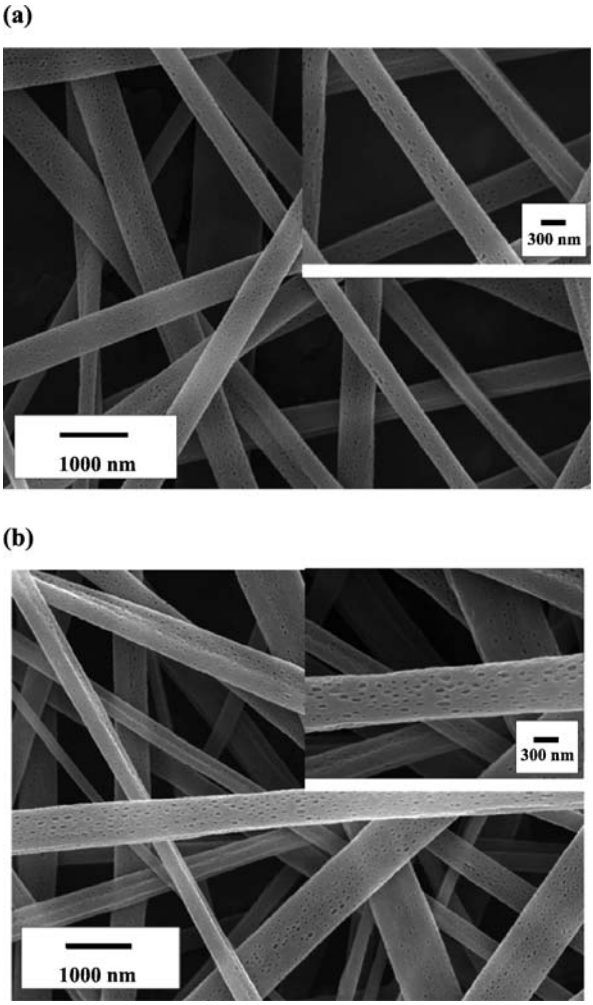

Fig. 34 SEM images of PF8/PMMA blend electrospun nanofibers with **a** 10 and **b** 50 wt. % of PF8. Reprinted with permission from [145]. © (2007) by the American Chemical Society

also shown the nanowires can exhibit a large fraction of β-type phase when PF8 is used [141]. It may well be that by placing PF8 into confined geometries one can achieve some degree of additional control over the phase that forms.

PF nanofibers are a second example of a top-down nanostructure. These fibers are conveniently prepared by electrospinning [143, 144], a technique applied to PFs in work by Chen et al. [145] and Jenekhe et al. [146]. An example of PF8 nanofibers is shown in Fig. 34. In this study various different PFs were blended with PMMA and depending on the molar ratio and mother solution used, either uniform or core-shell structures were obtained. PF ag-

gregation in the electrospun fibers appears to be much smaller than that in the spin-coated films due to the geometrical confinement of the electrospinning process and this leads to higher luminescence efficiency. The fibers with PMMA demonstrate a full light-emitting spectrum as a function of composition [145]. Moreover, a blend of PF8 and MEH-PPV is utilized in the fabrication of field-effect transistors [146].

5 Conclusions and Outlook

PFs, and conducting polymers in general, exhibit an enormously complex range of structural behavior with a polymer specific hierarchal self-assembly spanning many different length scales. In a few archetypal systems, primarily PF2/6 and PF8, it has been possible to provide both a theoretical or modeling framework for understanding the origin of some of these structural forms and the phase behavior. At times it is necessary to analyze the structure starting at the molecular level but, in some cases, a coarser grain analyses has proven effective in providing appreciable insight. Ideally one would like a generalizable and self-consistent methodology that could scale from microscopic to macroscopic length scales given that much CP behavior originates at nanometer distances. Moreover such methods would greatly improve the strategies available for efficient molecular design and engineering. At the larger length scales PFs are necessarily influenced by both the device environment and operation. Thus, there should be an increased emphasis on in-situ investigations. The current range of structural studies has already given critical input for many areas of PF research, synthetic chemistry in particular has benefited. These studies also continue to have major implications for optoelectronic applications. Examples include photovoltaic cells, LEDs, FETs, and biosensors. As already noted, the many reports in this review represent only the tip of the proverbial iceberg in terms of what has and what can be achieved. We expect that structure studies will continue to play a key role in the years to come.

References

1. Hoeben FJM, Jonkheijm P, Meijer EW, Schennig APHJ (2005) Chem Rev 105:1491
2. Winokur MJ, Chunwachirasiri W (2003) J Polym Sci B 41:2630
3. Winokur MJ (2007) In: Skotheim TA, Reynolds JR (eds) Handbook of Conducting Polymers. CRC Press LLC, Boca Raton, FL, p 1
4. Menzel H (1996) In: Salamone JC (ed) Polymer Materials Encyclopedia. CRC Press, Boca Raton, FL, p 2916
5. Grosberg AY, Khokhlov AR (1994) Statistical Physics of Macromolecules. American Institute of Physics, Woodbury, NY

6. de Gennes PG, Prost J (1998) The Physics of Liquid Crystals. Oxford University Press, Oxford
7. Grimsdale AC, Müllen K (2006) Adv Polym Sci 199:1
8. Knaapila M, Stepanyan R, Lyons BP, Torkkeli M, Monkman AP (2006) Adv Funct Mater 16:599
9. Neher D (2001) Macromol Rapid Commun 22:1365
10. Scherf U, List EJW (2002) Adv Mater 14:477
11. de Gennes P-G (1979) Scaling Concepts in Polymer Physics. Cornell University Press, Ithaca
12. Becker K, Lupton JM (2005) J Am Chem Soc 127:7306
13. Dubin F, Melet R, Barisien T, Grousson R, Legrand L, Schott M, Voliotis V (2006) Nat Phys 2:32
14. Guillet T, Berréhar J, Grousson R, Kovensky J, Lapersonne-Meyer C, Schott M, Voliotis V (2001) Phys Rev Lett 87:087401
15. Clark J, Silva C, Friend RH, Spano FC (2007) Phys Rev Lett 97:206406
16. Ariu M, Lidzey DG, Sims M, Cadby AJ, Lane PA, Bradley DDC (2002) J Phys Condens Matter 14:9975
17. Chunwaschirasiri W, Tanto B, Huber DL, Winokur MJ (2005) Phys Rev Lett 94:107402
18. Marcon V, van der Vegt N, Wegner G, Raos G (2006) J Phys Chem B 110:5253
19. Arif M, Volz C, Guha S (2006) Phys Rev Lett 96:025503
20. Volz C, Arif M, Guha S (2007) J Chem Phys 126:064905
21. Banach MJ, Friend RH, Sirringhaus H (2004) Macromolecules 37:6079
22. Grell M, Bradley DDC, Long X, Chamberlain T, Inbasekaran M, Woo EP, Soliman M (1998) Acta Polym 49:439
23. Fytas G, Nothofer HG, Scherf U, Vlassopoulos D, Meier G (2002) Macromolecules 35:481
24. Knaapila M, Stepanyan R, Torkkeli M, Lyons BP, Ikonen TP, Almásy L, Foreman JP, Serimaa R, Güntner R, Scherf U, Monkman AP (2005) Phys Rev E 71:041802
25. Knaapila M, Garamus VM, Dias FB, Almásy L, Galbrecht F, Charas A, Morgado J, Burrows HD, Scherf U, Monkman AP (2006) Macromolecules 39:6505
26. Somma E, Loppinet B, Chi C, Fytas G, Wegner G (2006) Phys Chem Chem Phys 8:2773
27. Dias FB, Knaapila M, Monkman AP, Burrows HD (2006) Macromolecules 39:1598
28. Wu L, Sato T, Tang H-Z, Fujiki M (2004) Macromolecules 37:6183
29. Kitts CC, Vanden Bout DA (2007) Polymer 48:2322
30. Dias FB, Morgado J, Macanita AL, da Costa FP, Burrows HD, Monkman AP (2006) Macromolecules 39:5854
31. Rahman MH, Chen C-Y, Liao S-C, Chen H-L, Tsao C-S, Chen J-H, Liao J-L, Ivanov VA, Chen S-A (2007) Macromolecules 40:6572
32. Knaapila M, Dias FB, Garamus VM, Almásy L, Torkkeli M, Leppänen K, Galbrecht F, Preis E, Burrows HD, Scherf U, Monkman AP (2007) Macromolecules 40:9398
33. Knaapila M, Almásy L, Garamus VM, Ramos ML, Justino LLG, Galbrecht F, Preis E, Schref U, Burrows HD, Monkman AP (2008) Polymer 49:2033
34. Levitsky IA, Kim J, Swager TM (2001) Macromolecules 34:2315
35. Chen L, McBranch DW, Wang H-L, Helgeson R, Wudl F, Whitten DG (1999) Proc Natl Acad Sci USA 96:12287
36. Sirringhaus H (2005) Adv Mater 17:2411
37. Gaylord BS, Heeger AJ, Bazan GC (2002) Proc Natl Acad Sci USA 99:10954
38. Chi C, Mikhailovsky A, Bazan GC (2007) J Am Chem Soc 129:11134

39. Baker ES, Hong JW, Gaylord BS, Bazan GC, Bowers MT (2006) J Am Chem Soc 128:8484
40. Xu Q-H, Gaylord BS, Wang S, Bazan GC, Moses D, Heeger AJ (2004) Proc Natl Acad Sci USA 101:11634
41. Liu B, Bazan GC (2005) Proc Natl Acad Sci USA 102:589
42. Wang H, Lu P, Wang B, Qiu S, Liu M, Hanif M, Cheng G, Liu S, Ma Y (2007) Macromol Rapid Commun 28:1645
43. Ma W, Iyer PK, Gong X, Liu B, Moses D, Bazan GC, Heeger AJ (2005) Adv Mater 17:274
44. Burrows HD, Lobo VMM, Pina J, Ramos ML, Seixas de Melo J, Valente AJM, Tapia MJ, Pradhan S, Scherf U (2004) Macromolecules 37:7425
45. Tapia MJ, Burrows HD, Knaapila M, Monkman AP, Arroyo A, Pradhan S, Scherf U, Pinazo A, Pérez L, Móran C (2006) Langmuir 22:10170
46. Tapia MJ, Burrows HD, Valente AJM, Pradhan S, Scherf U, Lobo VMM, Pina J, Seixas de Melo J (2005) J Phys Chem B 109:19108
47. Burrows HD, Tapia MJ, Silva CL, Pais AACC, Fonseca SM, Pina J, Seixas de Melo J, Wang Y, Marques EF, Knaapila M, Monkman AP, Garamus VM, Pradhan S, Scherf U (2007) J Phys Chem B 111:4401
48. Knaapila M, Almásy L, Garamus VM, Pearson C, Pradhan S, Petty MC, Scherf U, Burrows HD, Monkman AP (2006) J Phys Chem B 110:10248
49. Burrows HD, Knaapila M, Monkman AP, Tapia MJ, Fonseca SM, Ramos ML, Pyckhout-Hintzen W, Pradhan S, Scherf U (2008) J Phys Condens Matter 20:104210
50. Al Attar HA, Monkman AP (2007) J Phys Chem B 111:12418
51. Lieser G, Oda M, Miteva T, Meisel A, Nothofer H-G, Scherf U, Neher D (2000) Macromolecules 33:4490
52. Knaapila M, Lyons BP, Kisko K, Foreman JP, Vainio U, Mihaylova M, Seeck OH, Pålsson L-O, Serimaa R, Torkkeli M, Monkman AP (2003) J Phys Chem B 107:12425
53. Tanto B, Guha S, Martin CM, Scherf U, Winokur MJ (2004) Macromolecules 37:9438
54. Knaapila M, Kisko K, Lyons BP, Stepanyan R, Foreman JP, Seeck OH, Vainio U, Pålsson L-O, Serimaa R, Torkkeli M, Monkman AP (2004) J Phys Chem B 108:10711
55. Knaapila M, Stepanyan R, Lyons BP, Torkkeli M, Hase TPA, Serimaa R, Güntner R, Seeck OH, Scherf U, Monkman AP (2005) Macromolecules 38:2744
56. Knaapila M, Lyons BP, Hase TPA, Pearson C, Petty MC, Bouchenoire L, Thompson P, Serimaa R, Torkkeli M, Monkman AP (2005) Adv Funct Mater 15:1517
57. Chi C, Lieser G, Enkelmann V, Wegner G (2005) Macromol Chem Phys 206:1597
58. Guha S, Chandrasekhar M (2004) Phys Stat Sol 241:3318
59. Knaapila M, Torkkeli M, Monkman AP (2007) Macromolecules 40:3610
60. Stepanyan R, Subbotin A, Knaapila M, Ikkala O, ten Brinke G (2003) Macromolecules 36:3758
61. Blondin P, Bouchard J, Beaupré S, Belletête M, Durocher G, Leclerc M (2000) Macromolecules 33:5874
62. Craig MR, Jonkheijm P, Meskers SCJ, Schenning APHJ, Meijer EW (2003) Adv Mater 15:1435
63. Lakhwani G, Meskers SCJ, Janssen RAJ (2007) J Phys Chem B 111:5124
64. Koeckelberghs G, De Cremer L, Persoons A, Verbiest T (2007) Macromolecules 40:4173
65. Schilling T, Pronk S, Mulder B, Frenkel D (2005) Phys Rev E 71:036138
66. Martin CM, Guha S, Chandrasekhar M, Chandrasekhar HR, Guentner R, Scanduicci de Freitas P, Scherf U (2003) Phys Rev B 68:115203
67. Grell M, Bradley DDC, Ungar G, Hill J, Whitehead KS (1999) Macromolecules 32:5810

68. Ariu A, Lidzey DG, Bradley DDC (2000) Synth Met 111/112:607
69. Kawana S, Durrell M, Lu J, Macdonald JE, Grell M, Bradley DDC, Jukes PC, Jones RAL, Bennett SL (2002) Polymer 43:1907
70. Winokur MJ, Slinker J, Huber DL (2003) Phys Rev B 67:184106
71. Misaki M, Ueda Y, Nagamatsu S, Yoshida Y, Tanigaki N, Yase K (2004) Macromolecules 37:6926
72. Rothe C, King SM, Dias F, Monkman AP (2004) Phys Rev B 70:195213
73. Chen SH, Chou HL, Su AC, Chen SA (2004) Macromolecules 37:6833
74. Chen SH, Su AC, Chen SA (2005) J Phys Chem B 109:10067
75. Chen SH, Su AC, Su CH, Chen SA (2005) Macromolecules 38:379
76. Brinkmann M (2007) Macromolecules 40:7532
77. Donley CL, Zaumseil J, Andreasen JW, Nielsen MM, Sirringhaus H, Friend RH, Kim J-S (2005) J Am Chem Soc 127:12890
78. Kinder L, Kanicki J, Swensen J, Petroff P (2003) Proc SPIE Int Soc Opt Eng 5217:35
79. Schmidtke JP, Kim JS, Gerschner J, Silva C, Friend RH (2007) Phys Rev Lett 99:167401
80. Yang G-Z, Wang W-Z, Wang M, Liu T (2007) J Phys Chem B 111:7747
81. Chen SH, Su AC, Su CH, Chen SA (2006) J Phys Chem B 110:4007
82. Vamvounis G, Nyström D, Antoni P, Lindgren M, Holdcroft S, Hult A (2006) Langmuir 22:3959
83. Leclerc M, Ranger M, Bélanger-Gariépy F (1998) Acta Cryst C 54:799
84. McFarlene S, McDonald R, Veinot JGC (2006) Acta Cryst E 62:o859
85. Destri S, Pasini M, Botta C, Porzio W, Bertini F, Marchiò L (2002) J Mater Chem 12:924
86. Chi C, Im C, Enkelmann V, Ziegler A, Lieser G, Wegner G (2005) Chem Eur J 11:6833
87. Jo JH, Chi CY, Hoger S, Wegner G, Yoon DY (2004) Chem Eur J 10:2681
88. Geng Y, Trajkovska A, Katsis D, Ou JJ, Culligan SW, Chen SH (2002) J Am Chem Soc 124:8337
89. Güntner R, Farrell T, Scherf U, Miteva T, Yasuda A, Nelles G (2004) J Mater Chem 14:2622
90. Oda M, Nothofer H-G, Lieser G, Scherf U, Meskers SCJ, Neher D (2000) Adv Mater 12:362
91. Tsoi WC, Charas A, Cadby AJ, Khalil G, Adawi AM, Iragi A, Hunt B, Morgado J, Lidzey DG (2008) Adv Funct Mater 18:600
92. Sirringhaus H, Wilson RJ, Friend RH, Inbasekaran M, Wu W, Woo EP, Grell M, Bradley DDC (2000) Appl Phys Lett 77:406
93. Redecker M, Bradley DDC, Inbasekaran M, Woo EP (1999) Appl Phys Lett 74:1400
94. Yasuda T, Fujita K, Tsutsui T, Geng Y, Culligan SW, Chen SH (2005) Chem Mater 17:264
95. Grell M, Knoll W, Lupo D, Meisel A, Miteva T, Neher D, Nothofer H-G, Scherf U, Yasuda A (1999) Adv Mater 11:671
96. Grell M, Bradley DDC, Inbasekaran M, Woo EP (1997) Adv Mater 9:798
97. Lyons BP, Monkman AP (2004) J Appl Phys 96:4735
98. Tammer M, Monkman AP (2002) Adv Mater 14:210
99. Ramsdale CM, Greenham NC (2002) Adv Mater 14:212
100. King SM, Vaughan HL, Monkman AP (2007) Chem Phys Lett 440:268
101. Gather MC, Bradley DDC (2007) Adv Funct Mater 17:749
102. Winokur MJ, Cheun H, Knaapila M, Monkman A, Scherf U (2007) Phys Rev B 75:113202

103. Sirringhaus H, Brown PJ, Friend RH, Nielsen NM, Bechgaard K, Langeveld-Voss BMW, Spiering AJH, Janssen RAJ, Meijer EW, Herwig P, de Leeuw DMR (1999) Nature 401:685
104. Galambosi S, Knaapila M, Soininen AJ, Nygård K, Huotari S, Galbrecht F, Scherf U, Monkman AP, Hämäläinen K (2006) Macromolecules 39:9261
105. Grell M, Knoll W, Lupo D, Meisel A, Miteva T, Neher D, Nothofer H-G, Scherf U, Yasuda A (1999) Adv Mater 11:671
106. Miteva T, Meisel A, Nothofer H-G, Scherf U, Knoll W, Neher D, Grell M, Lupo D, Yasuda A (1999) Proc SPIE Int Soc Opt Eng 3797:231
107. Miteva T, Meisel A, Grell M, Nothofer HG, Lupo D, Yasuda A, Knoll W, Kloppenburg L, Bunz UHF, Scherf U, Neher D (2000) Synth Met 111-112:173
108. Nothofer H-G, Meisel A, Miteva T, Neher D, Forster M, Oda M, Lieser G, Sainova D, Yasuda A, Lupo D, Knoll W, Scherf U (2000) Macromol Symp 154:139
109. Lupo D, Yasuda A, Grell M, Neher D, Miteva T (2000) Polyimide Layer Comprising Functional Material, Device Employing the Polyimide Layer, Manufacturing the Device, Eur Pat Appl. Sony International (Europe) GmbH 10785 Berlin (DE), Max Planck Institut für Polymerforschung 55128 Mainz (DE), EP 1 011 154, p 29
110. Meisel A, Miteva T, Glaser G, Scheumann V, Neher D (2002) Polymer 43:5235
111. Banach MJ, Friend RH, Sirringhaus H (2003) Macromolecules 36:2838
112. Worsfold O, Hill J, Heriot SY, Fox AM, Bradley DDC, Richardson TH (2003) Mater Sci Eng C 23:541
113. Godbert N, Burn PL, Gilmour S, Markham JPJ, Samuel IDW (2003) Appl Phys Lett 89:5347
114. Cheun H, Liu X, Himpsel FJ, Knaapila M, Scherf U, Torkkeli M, Winokur MJ (2008) Macromolecules (submitted)
115. Knaapila M, Hase TPA, Torkkeli M, Stepanyan R, Bouchenoire L, Cheun H-S, Winokur MJ, Monkman AP (2007) Cryst Growth Des 7:1706
116. Knaapila M, Torkkeli M, Lyons BP, Hunt MRC, Hase TPA, Seeck OH, Bouchenoire L, Serimaa R, Monkman AP (2006) Phys Rev B 74:214203
117. Khokhlov AR (1991) Theories based on the Onsager Approach. In: Ciferri A (ed) Liquid Crystallinity in Polymers. VCH Publishers, New York, p 97
118. Rozanski LJ, Cone CW, Ostrowski DP, Vanden Bout DA (2007) Macromolecules 40:4524
119. Snaith HJ, Arias AC, Morteani AC, Silva C, Friend RH (2002) Nano Lett 2:1353
120. Snaith HJ, Friend RH (2004) Thin Solid Films 451/452:567
121. Teetsov J, Vanden Bout DA (2000) J Phys Chem B 104:9378
122. Teetsov J, Vanden Bout DA (2002) Langmuir 18:897
123. Teetsov JA, Vanden Bout DA (2001) J Am Chem Soc 123:3605
124. Surin M, Hennebicq E, Ego C, Marsitzky D, Grimsdale AC, Müllen K, Brédas J-L, Lazzaroni R, Leclère P (2004) Chem Mater 16:994
125. Chen S-H, Su A-C, Chen S-A (2006) Macromolecules 39:9143
126. Asawapirom U, Güntner R, Forster M, Scherf U (2005) Thin Solid Films 477:48
127. Tu G, Li H, Forster M, Heiderhoff R, Balk LJ, Sigel R, Scherf U (2007) Small 3:1001
128. Kong X, Jenekhe SA (2004) Macromolecules 37:8180
129. Kulkarni AP, Jenekhe SA (2003) Macromolecules 36:5285
130. Biagioni P, Celebrano M, Zavelani-Rossi M, Polli D, Labardi M, Lanzani G, Cerullo G, Finazzi M, Duo L (2007) Appl Phys Lett 91:191118
131. Arias AC, MacKenzie JD, Stevenson R, Halls JJM, Inbasekaran M, Woo EP, Richards D, Friend RH (2001) Macromolecules 34:6005

132. Xia Y, Friend RH (2005) Macromolecules 38:6466
133. Cadby AJ, Dean R, Elliott C, Jones RAL, Fox AM, Lidzey DG (2007) Adv Mater 19:107
134. Higgins AM, Martin SJ, Goghegan M, Heriot SY, Thompson RL, Cubitt R, Dalgliesh RM, Grizzi I, Jones RAL (2006) Macromolecules 39:6699
135. Morgado J, Moons E, Friend RH, Cacialli F (2000) Adv Mater 13:810
136. Charas A, Alves H, Alcácer L, Morgado J (2006) Appl Phys Lett 89:143519
137. Farrar SR, Contoret AEA, O'Neill M, Nicholls JE, Richards GJ, Kelly SM (2002) Phys Rev B 66:125107
138. Inaoka S, Roitman DB, Advincula RC (2005) Chem Mater 17:6781
139. O'Brien GA, Quinn AJ, Tanner DA, Redmond G (2006) Adv Mater 18:2379
140. O'Carroll D, Irwin J, Tanner DA, Redmond G (2007) Mater Sci Eng B 147:298
141. O'Carroll D, Iacopino D, O'Riordan A, Lovera P, O'Connor É, O'Brien GA, Redmond G (2008) Adv Mater 20:42
142. Moynihan S, Iacopino D, O'Carroll D, Lovera D, Redmond G (2008) Chem Mater 20:996
143. Pinto NJ, Johnson AT Jr, MacDiarmid AG, Mueller CH, Theofylaktos N, Robinson DC, Miranda FA (2003) Appl Phys Lett 83:4244
144. Reneker DH, Chun I (1996) Nanotechnology 7:216
145. Kuo C-C, Lin CH, Chen W-C (2007) Macromolecules 40:6959
146. Babel A, Li D, Xia Y, Jenkhe SA (2005) Macromolecules 38:4705